



Spectroscopic evaluation and fluorescence dynamics of several erbium doped laser materials
by Bruce Farris

A dissertation submitted in partial fulfillment of the requirements for the degree of Doctor of
Philosophy in Chemistry
Montana State University
© Copyright by Bruce Farris (2001)

Abstract:

Spectroscopic analysis and kinetic modeling of relaxation processes have been completed for 2.1% and 4% Er:YAG, 2% Er:YSO, and 0.5% Er:LuAG at room temperature. Simultaneously time and frequency resolved emission spectra were obtained using step scan Fourier transform spectroscopy. Experimental emission lifetimes of the $4I_{13/2}$, $4I_{11/2}$, and $4S_{3/2}$ levels were obtained directly from these spectra. The $4I_{13/2}$ lifetimes were found to be 6.6, 6.5, 8.6, and 5.7 msec for 2.1% and 4% Er:YAG, 2% Er:YSO, and 0.5% Er:LuAG, respectively. Lifetimes of 67.3, 10.5, and 67.7 μ sec were observed for 4% Er:YAG, 2% Er:YSO, and 0.5% Er:LuAG, respectively for the $4I_{11/2}$ state. Experimental lifetimes of 10.7, 3.5, and 12.3 μ sec were observed for the $4S_{3/2}$ state in 4% Er:YAG, 2% Er:YSO, and 0.5% Er:LuAG.

Quantum-mechanical calculations using Morrison's code were performed and theoretical radiative rates were generated. Comparison of these values with experimental emission lifetimes allowed determination of non-radiative relaxation rates and branching ratios.

Additionally, an experimentally based new method of determining non-radiative rates was developed that utilizes the intensity "volume" under the three-dimensional emission bands. The two methods provided good agreement.

Finally, the rate constants obtained by these methods were plugged into a set of coupled differential equations and numerically solved using the fifth order Runge-Kutta method in Mathematica. Good agreement with the experimental temporal behavior was obtained (including emission rises as well as decays) indicating the validity of the results. Non-radiative vs. radiative branching ratios were approximately equal for the first excited state $4I_{13/2}$, but higher electronic states typically showed > 99% of the population relaxing via the non-radiative channel.

SPECTROSCOPIC EVALUATION AND FLUORESCENCE DYNAMICS
OF SEVERAL ERBIUM DOPED LASER MATERIALS

by

Bruce Farris

A dissertation submitted in partial fulfillment
of the requirements for the degree

of

Doctor of Philosophy

in

Chemistry

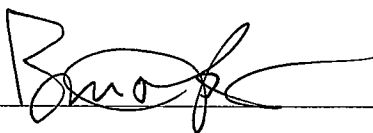
MONTANA STATE UNIVERSITY
Bozeman, Montana

July 2001

STATEMENT OF PERMISSION TO USE

In presenting this dissertation in partial fulfillment of the requirements for a doctoral degree at Montana State University, I agree that the Library shall make it available to borrowers under rules of the Library. I further agree that copying of this dissertation is allowable only for scholarly purposes, consistent with "fair use" as prescribed in the U.S. Copyright Law. Requests for extensive copying or reproduction of this dissertation should be referred to Bell & Howell Information and Learning, 300 North Zeeb Road, Ann Arbor, Michigan 48106, to whom I have granted "the exclusive right to reproduce and distribute my abstract in any format in whole or in part."

Signature



Date

19 July 2001

ACKNOWLEDGEMENTS

I would first like to thank my advising professor, Dr. Lee Spangler, for his support of my graduate study. Not only did he serve as an excellent teacher and research mentor, but he demonstrated extraordinary flexibility and support as I completed this work after accepting an opportunity to teach at Lansing Community College in Michigan. I would also like to thank the other members of my committee; Professors Edwin Abbott, Patrik Callis, Rufus Cone, Jack Riesselman, and Jan Sunner. This work would not have been possible without the other members of the Spangler research group; particularly Rich Martoglio, Tony Smith, and Wendi Sonnenberg for their involvement in other phases of the project. Additionally, I would like to express my gratitude to Dr. Reed Howald for his help and guidance on the kinetics portion of this work. Thank you to Dr. Michele McGuirl for the friendship and opportunity to discuss the project with a scientist that was not familiar with my work, providing a valuable perspective.

Also, I would like to thank my parents, Joe and Wiletta Farris, and my parents-in-law, Merle and Bonnie Johnson, for their support during my time in Montana. Thanks also to Benny Farris for motivating me to get away occasionally for much needed "sanity breaks"! Most of all, I'd like to thank my wife, Leslie, for her help, support, and extraordinary patience while I was completing this work.

TABLE OF CONTENTS

1. INTRODUCTION	1
Energy Levels in Erbium Laser Materials	1
Characterization of Laser Materials	4
Quantum-Mechanical Model	7
2. EXPERIMENTAL PROCEDURE	11
Overall Method of Analysis	11
Samples	13
Equipment and Techniques	14
Absorption	15
Emission	17
Temporally Resolved Emission	18
Temporally Resolved FT Spectroscopy	20
3. EXPERIMENTAL RESULTS	27
Absorption	27
Continuous Emission	36
IR Emission	38
Visible Emission	41
Temporally Resolved Emission	41
Er:YSO	49
Er:YAG	56
Er:LuAG	60
4. DISCUSSION OF RESULTS	72
Generation of Experimental Decay Curves	72
Discussion of Long Term Curvature in Log Plots	73
Kinetic Modeling of Experimental Data	77
$^4I_{11/2}$ Excitation	78
Summary of Total Volume Modeling Method	85
$^4S_{3/2}$ Excitation	91
5. SUMMARY	104
REFERENCES CITED	109

APPENDIX A: PROCEDURES USED IN QUANTUM-MECHANICAL MODELING
OF LASER MATERIALS 115

LIST OF TABLES

Table	Page
1. Excitation Frequencies for 2% Er:YSO	49
2. Excitation Frequencies for 4% Er:YAG	56
3. Absorption Transition Frequencies in Er ³⁺ Doped Materials (cm ⁻¹)	68
4. Experimental Lifetimes of Transitions in Erbium Doped Materials	71
5. Radiative Branching Ratios Calculated from Experimental Data	71
6. Branching Ratios for Decay from ⁴ I _{11/2} Manifold in 4% Er:YAG	83
7. Branching Ratios for ⁴ I _{11/2} Manifold in 2% Er:YSO or 0.5% Er:LuAG	83
8. Rate Constants for Relaxation following ⁴ I _{11/2} Pumping (μsec ⁻¹)	84
9. Branching Ratios for Decay from the ⁴ S _{3/2} and ⁴ I _{11/2} Manifolds in 4% Er:YAG following ⁴ S _{3/2} Excitation	94
10. Branching Ratios for Decay from the ⁴ S _{3/2} and ⁴ I _{11/2} Manifolds in 2% Er:YSO following ⁴ S _{3/2} Excitation	95
11. Branching Ratios for Decay from the ⁴ S _{3/2} and ⁴ I _{11/2} Manifolds in 0.5% Er:LuAG following ⁴ S _{3/2} Excitation	96
12. Rate Constants for Relaxation following ⁴ S _{3/2} Pumping (μsec ⁻¹)	97

LIST OF FIGURES

Figure	Page
1. Free Ion Energy Levels for the Er^{3+} Ion.....	3
2. Experimental Set-up for Absorption and Emission.....	16
3. Response Curves for Detector/Beamsplitter Combinations.....	17
4. Formation of the Interferogram in Step-Scan Mode.....	22
5. Time Resolved Spectrum Exhibiting Broadband Systematic Noise.....	24
6. Illustration of Systematic Noise Introduced by Source Pulse Instability.....	25
7. IR (top) and Visible Absorption Spectra of Er:YAG.....	29
8. IR (top) and Visible Absorption Spectra of Er:LuAG.....	30
9. Unoriented IR (top) and Visible Absorption Spectra of Er:YSO.....	31
10. IR Absorption Spectra of Er:YSO for Light Polarized Parallel to the $\langle 010 \rangle$, D_1 , and D_2 Directions.....	32
11. Visible Absorption Spectra of Er:YSO for Light Polarized Parallel to the $\langle 010 \rangle$, D_1 , and D_2 Directions.....	33
12. Absorption Transitions Observed in Figures 7-11.....	34
13. Radiative Emission Transitions Observed for ${}^4F_{9/2}$ and ${}^4F_{7/2}$ Excitation.....	38

14. IR Emission Spectrum of Er:YAG Pumped to the ${}^4F_{9/2}$ Manifold	39
15. IR Emission Spectrum of Er:YSO Pumped to the ${}^4F_{9/2}$ Manifold	40
16. IR Emission Spectrum of Er:YAG Pumped to the ${}^4F_{7/2}$ Manifold	42
17. IR Emission Spectrum of Er:YSO Pumped to the ${}^4F_{7/2}$ Manifold	43
18. Visible Emission Spectra of Er:YAG (top) and Er:YSO Pumped to the ${}^4F_{7/2}$ Manifold.....	44
19. Temporally Resolved Emission of Er:YSO Following Excitation to the ${}^4I_{13/2}$ Manifold	46
20. Temporally Resolved Emission of Er:YSO Following Excitation to the ${}^4I_{11/2}$ Manifold	47
21. Temporally Resolved Emission of Er:YSO Following Excitation to the ${}^4F_{7/2}$ Manifold.....	48
22. Decay (top) and Log of Intensity for the ${}^4I_{13/2} \rightarrow {}^4I_{15/2}$ Transition in 2% Er:YSO	51
23. Decay of Emission Transitions Originating from the ${}^4I_{11/2}$ Manifold in 2% Er:YSO	53
24. Log of Intensity of Emission Transitions Originating from the ${}^4I_{11/2}$ Manifold in 2% Er:YSO.....	54
25. Decay (top) and Log of Intensity of Emission Transitions Originating from the ${}^4S_{3/2}$ Manifold in 2% Er:YSO.....	57
26. Decay of the ${}^4I_{13/2} \rightarrow {}^4I_{15/2}$ Transition for 2.1% and 4% Er:YAG	58
27. Log of Intensity of the ${}^4I_{13/2} \rightarrow {}^4I_{15/2}$ Emission Transition in 2.1% and 4% Er:YAG	58

28. Decay (top) and Log of Intensity of Emission Transitions Originating from the $^4I_{11/2}$ Manifold in 4% Er:YAG	61
29. Decay (top) and Log of Intensity of Emission Transitions Originating from the $^4S_{3/2}$ Manifold in 4% Er:YAG	62
30. Decay of the $^4I_{13/2} \rightarrow ^4I_{15/2}$ Transition for 0.5% Er:LuAG	63
31. Decay (top) and Log of Intensity of the $^4I_{11/2}$ $\rightarrow ^4I_{15/2}$ Transition in 0.5% Er:LuAG	65
32. Decay (top) and Log of Intensity of the $^4S_{3/2}$ $\rightarrow ^4I_{13/2}$ Transition in 0.5% Er:LuAG	66
33. Rise of the $^4I_{13/2} \rightarrow ^4I_{15/2}$ Transition for Er^{3+} in Three Crystal Hosts.....	67
34. Illustration of Integration Method Used to Generate Decay Traces	74
35. Curvature Observed in Logarithmic Plots of Emission Decays	75
36. Data from Figure 35 After Addition of a Constant Value to the Decay Trace Data for Baseline Correction.....	77
37. Decay Processes Following $^4I_{11/2}$ Excitation.....	78
38. Linear (top) and Log Plots of Decay from the $^4I_{13/2}$ Manifold (Level 1) of 4% Er:YAG	87
39. Linear (top) and Log Plots of Decay from the $^4I_{11/2}$ Manifold (Level 2) of 4% Er:YAG	88
40. Logarithmic Plots of Decay from the $^4I_{11/2}$ Manifold (top) and $^4I_{13/2}$ Manifold of 0.5% Er:LuAG	89

41. Logarithmic Plots of Decay from the ${}^4I_{11/2}$ Manifold (top) and ${}^4I_{13/2}$ Manifold of 2% Er:YSO.....	90
42. Decay Processes Following ${}^4S_{3/2}$ Excitation	93
43. Linear (top) and Log Plots of Decay from the ${}^4I_{13/2}$ Manifold (Level 1) of 2% Er:YSO	99
44. Linear (top) and Log Plots of Decay from the ${}^4I_{11/2}$ Manifold (Level 2) of 2% Er:YSO	100
45. Linear (top) and Log Plots of Decay from the ${}^4S_{3/2}$ Manifold (Level 5) of 2% Er:YSO.....	101
46. Log Plots of Decay from the ${}^4I_{13/2}$ (top), ${}^4I_{11/2}$ (center), and ${}^4S_{3/2}$ Manifolds of 4% Er:YAG	102
47. Log Plots of Decay from the ${}^4I_{13/2}$ (top), ${}^4I_{11/2}$ (center), and ${}^4S_{3/2}$ Manifold of 0.5% Er:LuAG	103
A1. Flowsheet for Calculations When Experimental Energy Level Data are Available.....	118
A2. Flowsheet for Calculations When Experimental Energy Level Data for the Rare Earth Ion in a Similar Host are Available.....	119

ABSTRACT

Spectroscopic analysis and kinetic modeling of relaxation processes have been completed for 2.1% and 4% Er:YAG, 2% Er:YSO, and 0.5% Er:LuAG at room temperature. Simultaneously time and frequency resolved emission spectra were obtained using step scan Fourier transform spectroscopy. Experimental emission lifetimes of the ${}^4I_{13/2}$, ${}^4I_{11/2}$, and ${}^4S_{3/2}$ levels were obtained directly from these spectra. The ${}^4I_{13/2}$ lifetimes were found to be 6.6, 6.5, 8.6, and 5.7 msec for 2.1% and 4% Er:YAG, 2% Er:YSO, and 0.5% Er:LuAG, respectively. Lifetimes of 67.3, 10.5, and 67.7 μ sec were observed for 4% Er:YAG, 2% Er:YSO, and 0.5% Er:LuAG, respectively for the ${}^4I_{11/2}$ state. Experimental lifetimes of 10.7, 3.5, and 12.3 μ sec were observed for the ${}^4S_{3/2}$ state in 4% Er:YAG, 2% Er:YSO, and 0.5% Er:LuAG.

Quantum-mechanical calculations using Morrison's code were performed and theoretical radiative rates were generated. Comparison of these values with experimental emission lifetimes allowed determination of non-radiative relaxation rates and branching ratios.

Additionally, an experimentally based new method of determining non-radiative rates was developed that utilizes the intensity "volume" under the three-dimensional emission bands. The two methods provided good agreement.

Finally, the rate constants obtained by these methods were plugged into a set of coupled differential equations and numerically solved using the fifth order Runge-Kutta method in Mathematica. Good agreement with the experimental temporal behavior was obtained (including emission *rises* as well as decays) indicating the validity of the results. Non-radiative vs. radiative branching ratios were approximately equal for the first excited state ${}^4I_{13/2}$, but higher electronic states typically showed > 99% of the population relaxing via the non-radiative channel.

CHAPTER 1

INTRODUCTION

Erbium has been found to be a useful and versatile active atom for a variety of laser applications. It is capable of lasing near $3 \mu\text{m}$, a desirable wavelength for laser surgery, and around $1.7 \mu\text{m}$ in the eyesafe region (1,2). Lasing has also been achieved at several IR and visible wavelengths via upconversion processes (2-8). Erbium is often doped into solid-state crystalline hosts, which offer the benefits of durability, reliability, and convenience. For these reasons, there has been considerable interest in solid-state lasers using erbium as the active ion. Since the optical properties such as absorption and emission influence laser performance, spectroscopic investigation has been carried out on erbium in a wide variety of crystalline hosts (9-56). Additionally, lasing has been achieved in many solid state laser materials using erbium as the active lasing species. (2-11, 36, 45, 54-76).

Energy Levels in Erbium Laser Materials

Erbium, like all rare earth elements typically used as active lasing species, is most commonly incorporated into crystalline hosts in the trivalent

state. The resulting ground electron configuration of the Er^{3+} ion is a xenon-like electron structure with 11 additional electrons in the partially filled 4f orbitals ($[\text{Xe}] 4f^{11}$). The energy level structure of the erbium ion in crystalline hosts results from the Coulombic interaction of the 4f electrons with the nucleus and with each other, spin orbit coupling, and the host crystal field (77). The energy levels of the free Er^{3+} ion result from the electrostatic interaction and spin orbit coupling. The Coulombic interaction yields ^{2s+1}L terms, which are further split into J states by the spin-orbit interaction. The resulting free ion energy level diagram with the $^{2s+1}L_J$ states is shown in Figure 1, which includes the ground $^4I_{15/2}$ state through the seventh excited state ($^4F_{7/2}$). In actuality, the levels shown in Figure 1 are not pure $^{2s+1}L_J$ states, due to mixing of the levels. Each of the levels referred to by the $^{2s+1}L_J$ term symbol has other states mixed in. As can be seen by examination of the diagram, the free ion level separation is typically thousands of wavenumbers and transitions between the free ion levels are in the visible and infrared regions of the spectrum.

The host crystal field further splits each $^{2s+1}L_J$ term into a manifold of Stark levels. The degeneracy of the $^{2s+1}L_J$ states is $2J+1$, and this degeneracy is reduced by the crystal field splitting (77). The splitting is relatively small, with an overall manifold width of typically several hundred cm^{-1} , and a splitting between adjacent Stark levels of normally 50 - 100 cm^{-1} , due to the shielding of the 4f electrons from the host crystal field by the outer 5s and 5p

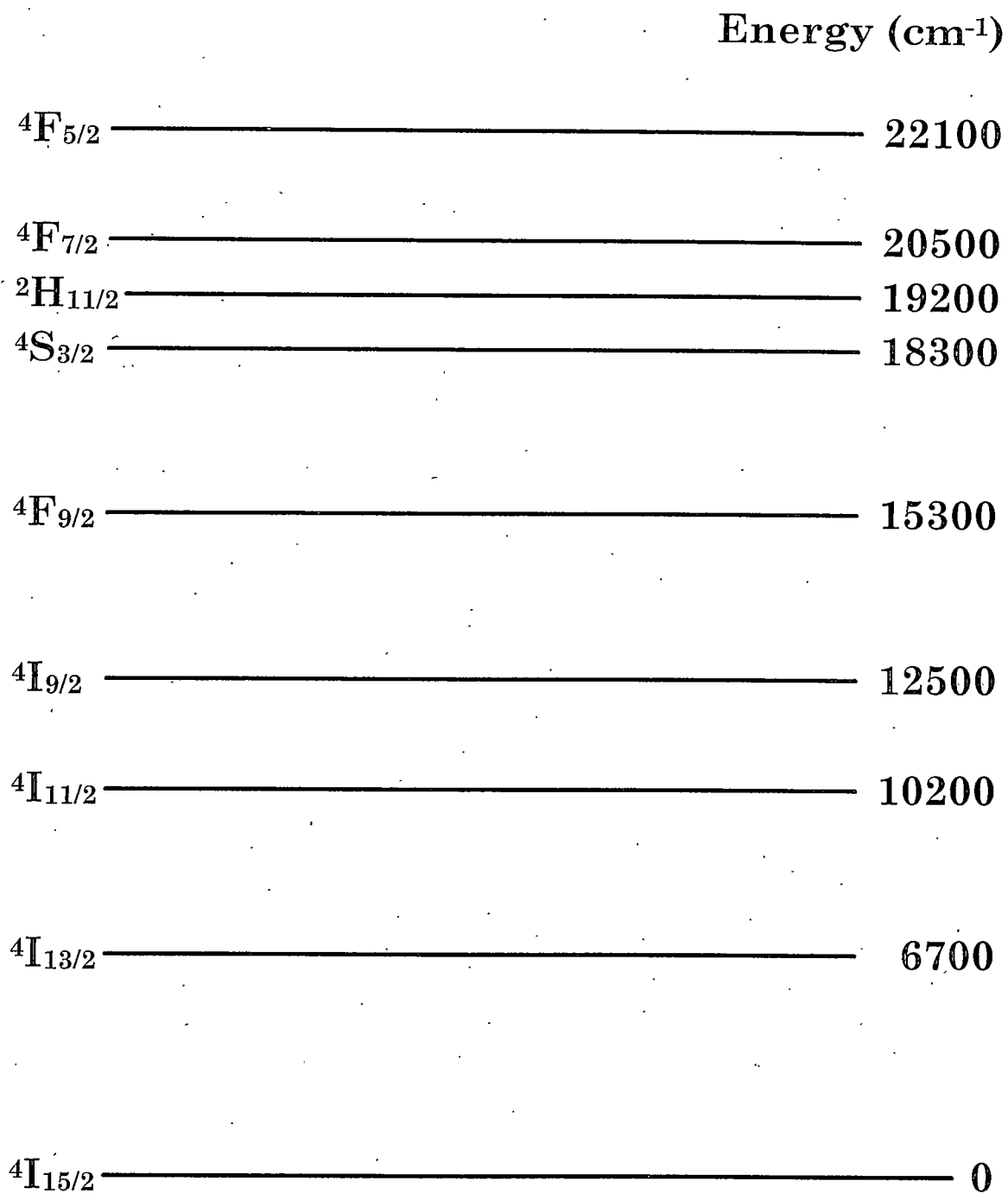


Figure 1. Free Ion Energy Levels for the Er³⁺ Ion.

electrons. The Stark level splitting can be exploited when a laser operating at a specific wavelength is desired. Coarse wavelength selection can be accomplished by choice of a specific rare earth ion, and fine "tuning" can be accomplished by selection of a host crystal that shifts the Stark levels such that the material is suited for the desired application. For that reason, Stark level assignment for different rare earth ions (including Er^{3+}) in crystalline hosts has historically been of interest, and a significant amount of work has been performed in this area for erbium(1,2,4,6,13,14,16,19-21,23,26,33,36,38-41,46,52,54,65).

Characterization of Laser Materials

The potential performance and operating characteristics of laser materials are to a large extent due to their spectroscopic properties. The absorption spectrum will determine potential pump wavelengths and influence pump efficiency, since pumping will be more efficient at strong absorption frequencies. After excitation has taken place, relaxation can occur via spontaneous radiative emission, nonradiative decay processes such as multiphonon relaxation, and/or ion-ion energy transfer processes. Radiative emissions can potentially be used as lasing transitions, and nonradiative

processes including energy transfer and multiphonon decay can enhance or detract from laser performance, depending upon the desired operating characteristics and pumping mechanism.

To ascertain the effect of the aforementioned properties on a particular lasing medium, it is useful to answer the following questions:

- What is the Stark level structure of the material?
- After excitation to a given manifold of Stark levels, what levels are involved in the relaxation process? Are these levels populated radiatively or nonradiatively? What levels are bypassed?
- Once populated, how is an excited state manifold depopulated? Is the manifold depopulated by radiative processes, nonradiative processes, or both? How quickly is it depopulated?
- What is the relative distribution (branching ratio) of the terminal levels of transitions originating from a particular manifold? What are the branching ratios of nonradiative relaxation processes?
- Do changes in dopant ion concentration (Er^{3+} in this study) or host crystal affect these population and/or depopulation processes?
- What, if any effects, are introduced by external factors such as temperature or excitation beam power?

Experimental methods or strategies that can answer some or all of these questions are of interest. Characterization of a material involves

absorption spectra, emission spectra resulting from continuous excitation to various manifolds, and temporally resolved emission spectra following modulated or pulsed excitation to the same manifolds. The absorption spectra are useful for determination of Stark level structure and identification of both excitation frequencies for emission experiments and pump frequencies for laser operation. The emission spectra provide information about the relaxation mechanisms from particular manifolds and identify promising laser transitions. The temporally resolved emission spectra provide information about the dynamics of both the radiative and nonradiative relaxation processes, which is of interest since the relative rates of population and depopulation of energy levels can affect whether and how well a material can function as a laser. For these reasons, these three experimental methods are all used in this study.

While spectroscopic study is useful in providing the previously mentioned information, combining it with complementary tools such as quantum-mechanical models and kinetic modeling using rate equations can increase its effectiveness. Emission spectra alone allow for direct observation of radiative emission transitions and provide some indirect information about nonradiative relaxation transitions. However, nonradiative relaxation rates and branching ratios can be gained by comparing experimentally determined lifetimes (which result from both radiative and nonradiative means of depopulation) with either low temperature or theoretically determined

radiative manifold lifetimes (which assume radiative processes are entirely responsible for depopulation). In this study, theoretical lifetimes are obtained from the quantum-mechanical model discussed in the next section. Alternatively, the rate and the relative contribution of the nonradiative relaxation processes can be determined by a newly developed method (presented in Chapter 4) that utilizes the intensity "volume" under the three dimensional emission bands of the temporally resolved spectra.

The kinetics of relaxation can be investigated by using the rate constants for the various relaxation processes (obtained by the experimental and/or theoretical methods discussed in the previous paragraph) following excitation to a particular level by solving sets of simultaneous rate equations for the involved energy levels. The combination of experimental methods, quantum-mechanical modeling, and kinetic modeling using rate equations can provide information that none of the three methods can provide alone, including information about processes that cannot be observed spectroscopically.

Quantum-Mechanical Model

A quantum-mechanical model developed by Morrison *et al* was used to calculate theoretical radiative lifetimes. The model is described in detail in Refs. 78-80 and is described briefly in this section.

Free ion wavefunctions are determined using a Hamiltonian that contains electrostatic, spin-orbit, and L^2 interactions (81). The host crystal field splits the free ion energy levels into Stark levels. Calculations of the Stark effects use a crystal field Hamiltonian of the form:

$$H_{CF} = \sum_i B_{nm} C_{nm}(i) \quad (1)$$

where the B_{nm} are crystal field parameters which describe the effect of the host crystal field on the free ion energy levels, the C_{nm} are spherical tensor operator components, nm covers the values of n and m allowed by the symmetry of the site of the rare earth in the host crystal, and the i summation is over all of the 4f electrons of the rare earth ion. The crystal field parameters are related to the crystal field components A_{nm} , which are spherical tensor components of the host crystal field at the ion site, calculated by a point charge lattice summation. The A_{nm} and B_{nm} are related by the radial factor ρ_n , which are primarily functions of the rare earth ion, though they can be influenced slightly by the host crystal, and the relationships:

$$B_{nm} = \rho_n A_{nm} \quad (2)$$

$$\rho_n = \frac{(B_{n0}^2 + 2B_{n2}^2 + 2B_{n4}^2 + \dots)^{1/2}}{(A_{n0}^2 + 2A_{n2}^2 + 2A_{n4}^2 + \dots)^{1/2}} \quad (3)$$

Stark levels for a rare earth ion in a particular host crystal can be calculated entirely from the theoretical model. To do so, host x-ray data can be used to determine A_{nm} and Equation 2 can be used with the newly

determined A_{nm} to calculate the crystal field parameters B_{nm} . The calculated B_{nm} can then be used with Equation 1 used to determine the crystal field Hamiltonian. Alternatively, if experimental energy levels are known, a set of B_{nm} can be fit to the experimental data. The B_{nm} from the fit can then be used along with the A_{nm} for the host and Equation 3 to calculate ρ_n , which are then used with A_{nm} for a similar host and Equation 2 to calculate B_{nm} for the similar host. By the second method, experimentally determined Stark levels for a rare earth ion in one host can be fit and used to calculate Stark levels for the same ion in the other hosts from the same "family" (i.e. the garnets) providing better results than purely theoretical calculations (1). The Morrison model is limited to low dopant concentrations, as it does not include the effect of the rare earth dopant ion on the host crystal (which would change the point charge lattice summation and the A_{nm} values).

The model can also be used to calculate theoretical emission transition probabilities, which means that theoretical radiative lifetimes of a particular energy level can be obtained as well, using the Judd - Ofelt treatment (82,83). In this treatment, the Judd-Ofelt parameters Ω_k (which contain the host dependent part of the electric dipole line strengths) can be calculated (39,79) and used to calculate the theoretical electric dipole line strength $S_{ed}(J \rightarrow J')$. The magnetic dipole line strength $S_{md}(J \rightarrow J')$, which is entirely dependent on the rare earth ion within the theory, is calculated from the theoretical magnetic dipole oscillator strength. The line strengths for each transition of

interest can then be related to the Einstein A coefficients for the respective transitions.

CHAPTER 2

EXPERIMENTAL PROCEDURE

In this chapter, the overall approach to analysis of the materials, including types of spectra collected and justification for collecting them, will be explained. Next, the discussion includes a description of the analyzed samples and the equipment and techniques utilized in obtaining the various spectra. The chapter concludes with a brief discussion of the temporally resolved Fourier Transform spectroscopic technique used to gather most of the data.

Overall Method of Analysis

We are interested in the various population and depopulation processes (both radiative and nonradiative) of the energy levels in erbium-doped laser materials. The project goal was to use several spectroscopic techniques to gain relevant information about these processes. First, absorption spectra were collected for each sample. Although absorption spectra of laser materials are of fundamental interest since they provide information on potential pump wavelengths for laser use, the more

immediate and practical use for the purposes of this project was to provide appropriate excitation frequencies of the samples for collection of emission spectra. While absorption spectra for Er:YAG (4,6,26,34,35,37,38,46), Er:LuAG (9), and Er:YSO (34,36,39,40), are well documented in the literature; it was still beneficial to run absorption on the specific samples analyzed to account for any impurities or anomalies.

Two different emission techniques were employed in this project: standard emission and temporally resolved emission. The standard emission spectra were obtained using a continuous excitation source, but source modulation was necessary to obtain the temporally resolved spectra. The standard emission spectra were obtained much more rapidly and conveniently than the temporally resolved spectra and provided sufficient information to make them worthwhile, even though the spectral information was reproduced in the temporally resolved emission spectra. First, the continuously pumped emission spectra were useful for initial identification and assignment of emission bands and their relative contribution toward depopulating higher energy levels after excitation. Secondly, they provided information useful in the setting up of the temporally resolved spectra. The longer-lived emission bands typically appeared stronger in the continuous spectra, so some very rough qualitative information on emission band lifetime could be extracted. However, this information is by no means conclusive since actual emission transition intensity must also be considered.

Finally, identification of emission bands by continuous spectra facilitated the setting up of appropriate wavelength ranges for temporally resolved spectroscopy.

In addition to providing the above-mentioned information, the temporally resolved emission spectra provided emission decay rates and allowed the deconvolution of multiple overlapping bands which were difficult to distinguish in the spectral dimension. Second, since emission bands with the same decay profiles likely originate from the same manifold, it provided more convincing evidence for the assignment of emission transitions. Third, comparing emission spectra excited at different frequencies yielded information about the nonradiative processes involved in deexcitation. Finally, the ability to pump several excited states of the sample and observe the "turning on and off" of emission bands helped identify the originating manifold of the emission transitions. These capabilities will be demonstrated in Chapters 3 and 4.

Samples

Scientific Materials Corporation provided the erbium-doped YSO, YAG, and LuAG samples analyzed in this project. The samples were discs cut from crystals grown by Scientific Materials and polished on the edges and faces. They are approximately one-eighth inch thick and range from 0.5 to 1.5

inches in diameter. Erbium ions occupy yttrium sites in both the YAG and YSO crystal lattices, while they occupy lutetium sites in LuAG. There are two inequivalent sites occupied by erbium in Er:YSO, and the YSO host has three principal axes of polarization (39). While both orientationally resolved and unoriented absorption spectra were obtained for Er:YSO, orientationally resolved emission spectra were not obtained since it has been determined that the contribution of the two erbium centers to emission (on the time scales studied in this work) does not depend on which one is pumped more efficiently. (39) Moncorge *et al* found that the fluorescence bandshapes were identical for all the pump wavelengths studied (it is expected that for a particular wavelength one site would be excited more efficiently than the other), indicating that energy transfer occurs on a sufficiently faster time scale than the emission transitions studied, which occur on the microsecond and millisecond time scales.

Equipment and Techniques

The need to conduct the various experiments discussed earlier in this chapter makes a versatile spectroscopic facility necessary. The equipment and experiment setups used in this project are nearly identical to those described by Richard Martoglio (a previous member of the Lee Spangler research group at Montana State University) in his thesis (84) detailing his

similar work with thulium-doped materials. These procedures will be briefly outlined in this section, and all differences from the equipment setups described by Martoglio will be discussed in detail. A general equipment layout is shown in Figure 2.

Absorption

Absorption experiments were carried out using the Bruker IFS66 Fourier Transform Spectrometer. The instrument, which was described in detail by Martoglio (84), utilizes a Michelson interferometer as its basic design. The source was a broadband tungsten lamp included in the spectrometer. Two different beamsplitters were used depending on the spectral range desired for the specific experiment: a calcium fluoride beamsplitter was generally used for lower frequency measurements and a quartz beamsplitter was utilized for higher frequency spectra. A liquid nitrogen cooled indium antimonide detector was utilized in the infrared, while visible detection was accomplished using a silicon diode. Figure 3 shows response curves for all four possible detector/beamsplitter combinations. The detector/beamsplitter combinations for all absorption and emission experiments were chosen to get the best signal response for the desired spectral region.

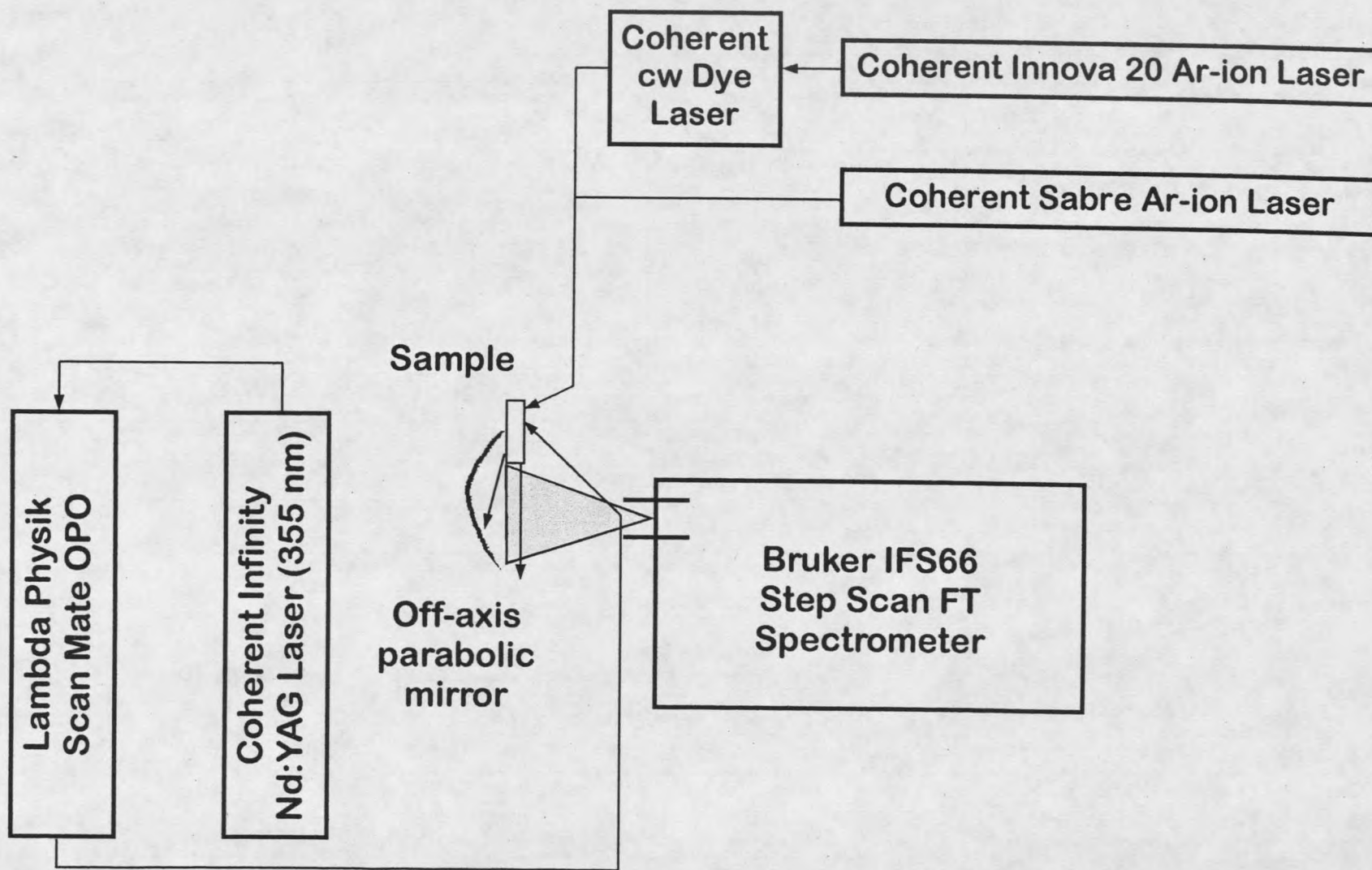


Figure 2. Experimental Set-up for Absorption and Emission.

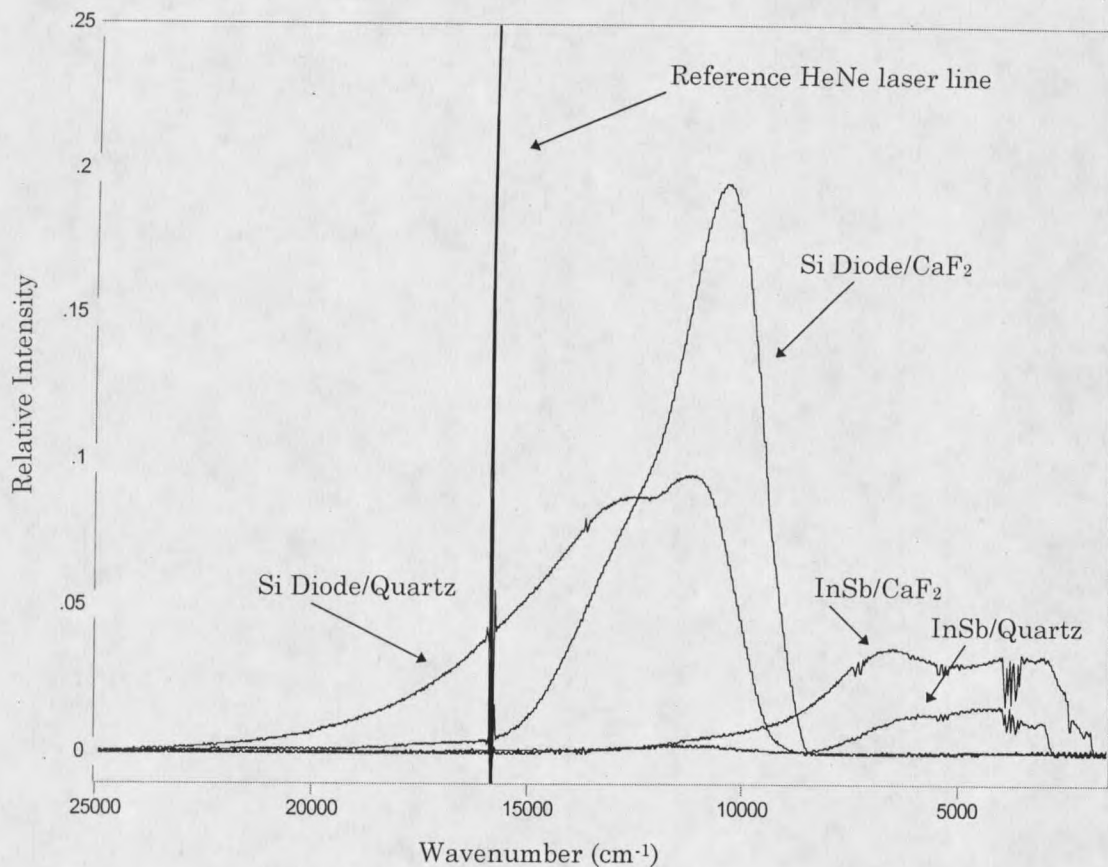


Figure 3: Response Curves for Detector/Beamsplitter Combinations.

Emission

An argon-ion laser provided a convenient excitation source for emission experiments since all the samples studied absorb the 488 nm line. Two different Ar-ion lasers were used as sources during the project. In addition to functioning directly as an excitation source, one of the Ar-ion lasers was also used to pump a Coherent continuous dye laser, allowing access to other erbium absorption bands.

The general emission setup is illustrated in Figure 2. After excitation by the Ar-ion laser, sample emission was collected by an off-axis parabolic mirror. The parabolic mirror was obtained from Bruker and was originally designed for light collection before entering the IFS66 spectrometer, thereby ensuring f-matching ($f/4.5$) to the IFS66. The sample was placed at the appropriate distance outside the interferometer to allow f-matching. Collecting the emission in the off-axis parabolic mirror improved emission signal-to-noise by a factor of approximately 40 over simply placing the sample in front of the IFS66 emission port, due to collection of a larger solid angle of the emitted radiation. Additionally, an aperture was sometimes placed at the IFS66 emission port to eliminate unwanted scattered laser light. The same beamsplitters and detectors used for absorption were used for the emission measurements, and optical filters were sometimes placed in the IFS66 absorption sample chamber to prevent unwanted emission signal and/or scattered source light from reaching the detector.

Temporally Resolved Emission

In this section, the equipment and setup for the temporally resolved emission experiments are discussed. The temporally resolved spectroscopic method is discussed in more detail in the next section.

Since source modulation was necessary to conduct the time-resolved experiments, the Ar-ion source (or Ar-ion pumped continuous dye laser) was

modulated using either a chopper (for millisecond pulses) or an acousto-optic modulator (for microsecond pulses) for the earlier experiments during the initial stages of the project.

A shorter excitation pulse was necessary to study the relaxation processes in these materials, many of which occur on the microsecond time scale or faster, thus nanosecond pulses were used for most of the temporally resolved work. The 1064 nm output from a Coherent Infinity Nd:YAG laser was tripled to 355 nm and used to pump a Lambda-Physik ScanMate OPO. The OPO could provide tunable output from 400 nm to nearly 2.5 microns, and output powers used were typically 2-5 mJ/pulse. With system repetition rates adjustable from 0.1 to 100 Hz, the Infinity/ScanMate combination provided the necessary flexibility to excite each different sample to a number of different electronic states. Additionally, the repetition rate could be set to allow for complete relaxation of the material before the next pulse was delivered.

The general experiment layout for the temporally resolved emission work was identical to the continuous emission setup (see Figure 2). When the Infinity/OPO excitation source was used, the beam was focused from approximately one cm to 2 mm in diameter using a $f/12$ lens (based on lens diameter) placed between the OPO outlet and the sample. The sample was placed at the focal point to maximize pump power density. Additionally, the sample placement was such that the excitation beam struck the sample near

the edge to minimize self absorption. The moving mirror in the Bruker interferometer was operated in step scan mode rather than rapid scan mode (this will be discussed further in the next section). Since the mirror was designed to be at a complete stop while gathering data, the system was susceptible to mechanical vibration. There are two major differences in the equipment setup used for gathering most of the time resolved data in this study with the setup employed by Martoglio. (84) First, the Infinity/OPO source was mounted on a larger optical table along with the interferometer. The optical table in use when Martoglio gathered his data was too small to accommodate the entire system. Tying the entire system together on one table greatly diminished the effect of building vibrations on the system, enhancing the signal-to-noise ratio. Additionally, the setup was moved to the Spangler group's temporary laboratory facility at Scientific Materials Corporation, which was located on the ground floor as opposed to the second floor laboratory in Gaines Hall at MSU. The overall building vibrations were less on the ground floor location, again providing improved mechanical stability and signal-to-noise ratio.

Temporally Resolved FT Spectroscopy

In this section, the temporally resolved Fourier Transform technique is briefly discussed. The technique is discussed in detail by Martoglio. (84)

In a standard Fourier Transform experiment using a Michelson interferometer, the moving mirror is scanned continuously on the order of 40 kHz, known as "rapid scan" mode. Temporal resolution at a given wavelength cannot be obtained in rapid scan mode because the mirror position changes during the course of the temporal event. However, operation of the IFS66 in step scan mode allows the user to obtain temporal information. In step scan mode, the moving mirror is stopped at each location and data is obtained. The method of obtaining data is illustrated on Figure 4. At each mirror position, the desired number of data points are obtained at a time interval corresponding to the desired temporal resolution. This process can be completed as many times as desired for signal averaging. Data corresponding to a particular mirror position is shown as a horizontal column in the first part of the figure. An interferogram is constructed using the data from each of the different mirror positions at one moment in time, known as a "time slice" (illustrated in the second part of Figure 4). This process is repeated for each of the time slices, resulting in a separate interferogram for each moment in time. The data needed for each of these interferograms is a vertical column in the first part of Figure 4. Each interferogram is then Fourier transformed to yield a spectrum for each time slice (last part of Figure 4), resulting in a temporally resolved emission spectrum.

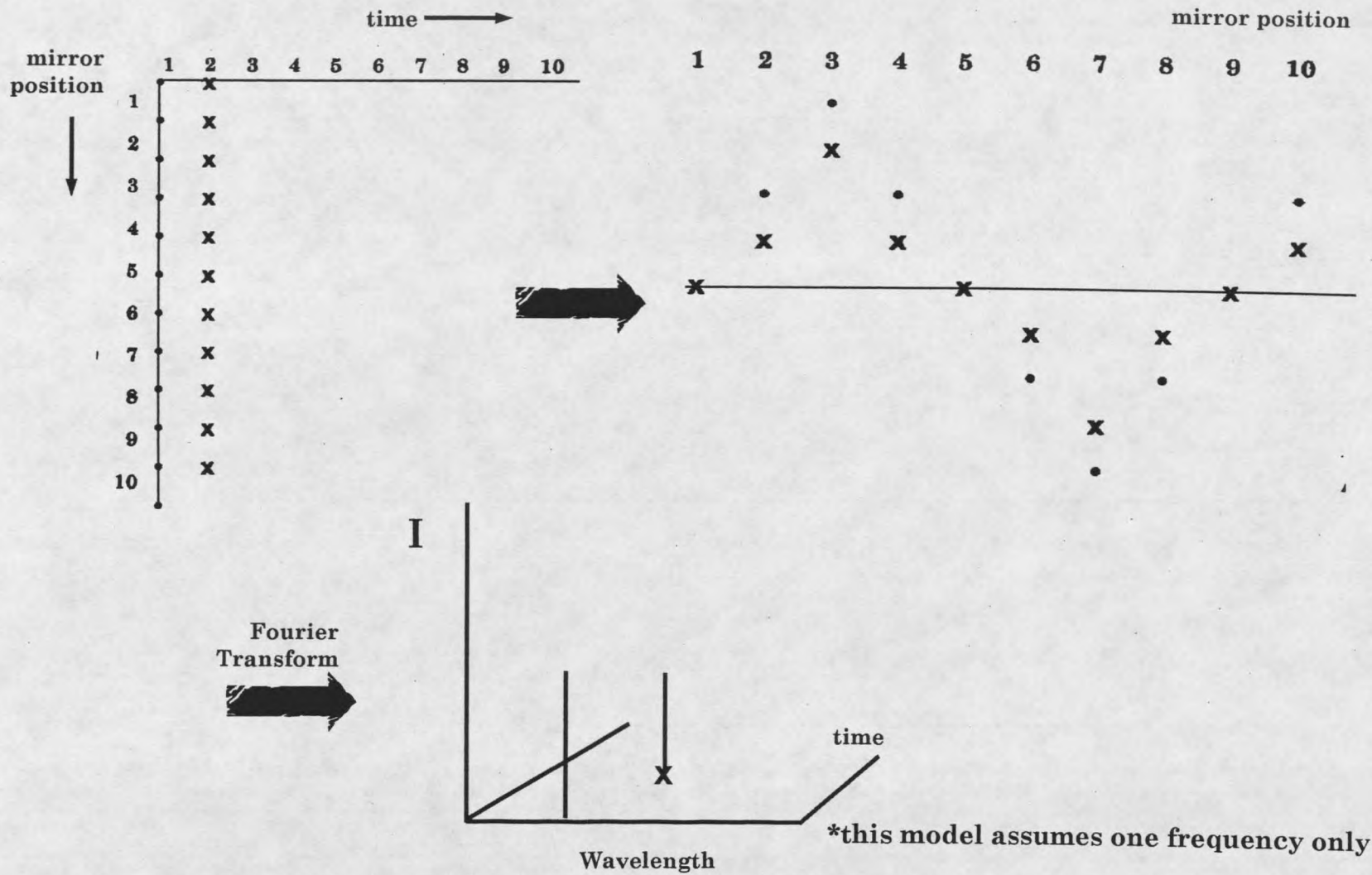


Figure 4. Formation of the Interferogram in Step-Scan Mode.

Intensity fluctuations in the Infinity/OPO source coupled with the time resolved FT method led to broadband baseline noise which decayed proportionately with the signal over time (see Figure 5). The way in which these fluctuations manifested themselves as broadband noise can most easily be seen by looking at the example of a single emission frequency (see Figure 6). If the emission intensity is the same for each mirror position, the interferogram will be a sine wave, which is Fourier transformed into a single frequency. Fluctuations in emission intensity lead to an interferogram that is not quite sinusoidal (see Figure 6). This nonsinusoidal interferogram is Fourier transformed into multiple frequencies, corresponding to the actual emission frequency and noise. This effect is of course compounded in emission from the erbium doped laser crystals, which have multiple emission bands as opposed to a single emission frequency. This effect can actually sometimes be beneficial since the noise from intensity fluctuations is spread over the whole spectral region rather than being concentrated over the emission band. However, it can be detrimental in the case where an emission spectrum contains both strong and weak bands, since noise from intensity fluctuations in the strong bands can obscure the weak bands.

Two actions were taken to address these noise issues. Increased signal averaging was the simplest solution, although it meant longer experiment times, leaving the experiment more susceptible to long-term fluctuations. Also, when it was desirable to examine a weaker emission band, stronger

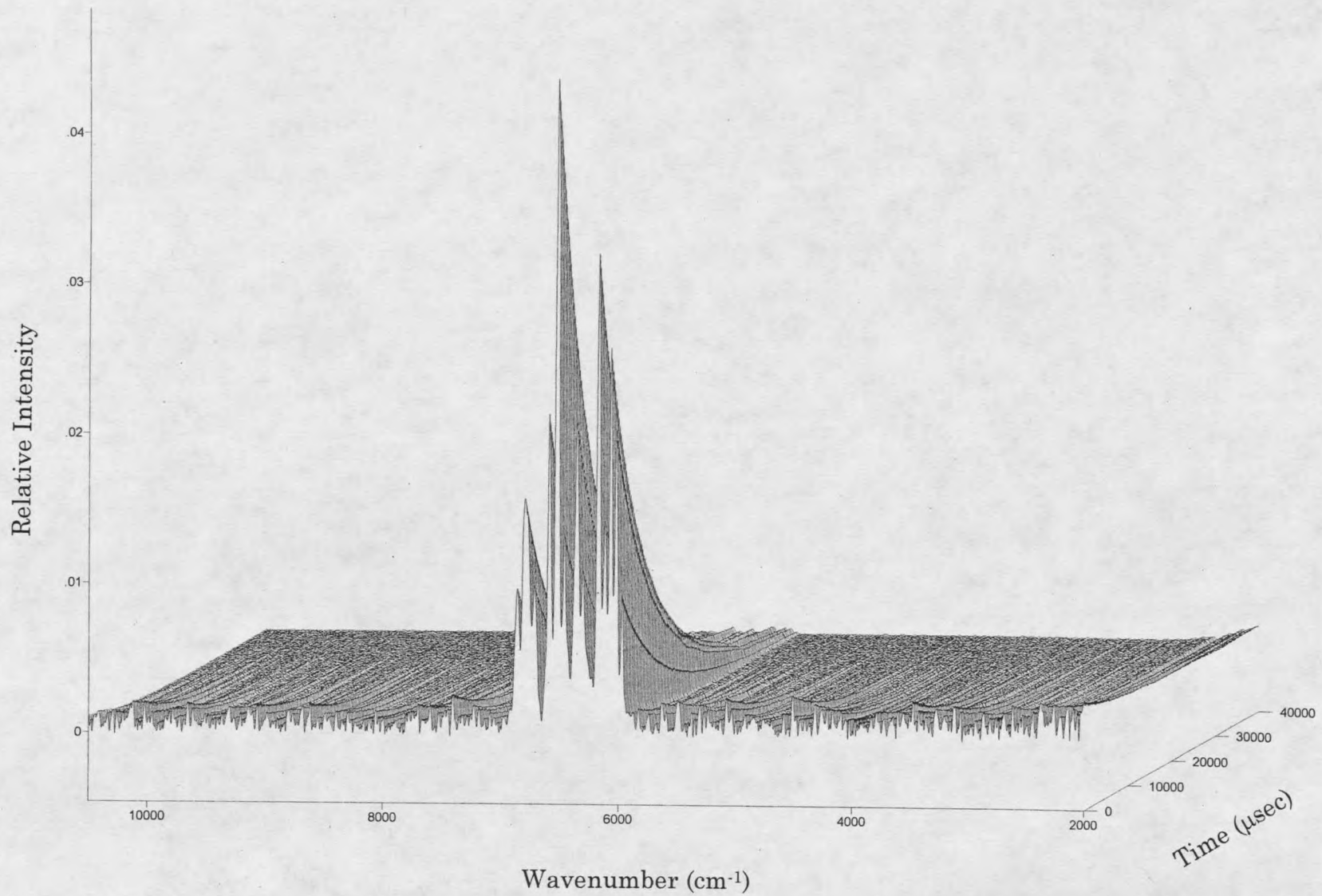
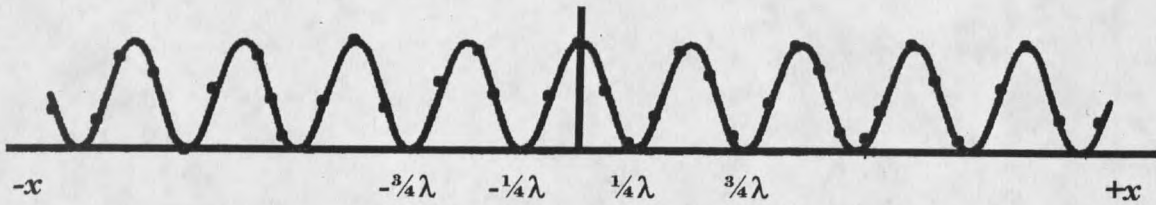
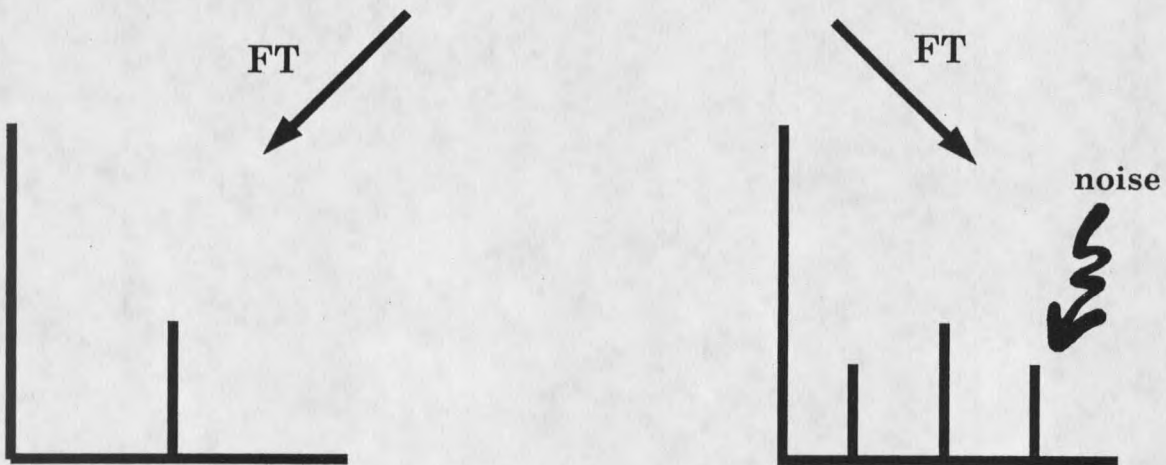


Figure 5. Time Resolved Spectrum Exhibiting Broadband Systematic Noise.

For a pulsed monochromatic source, if the intensity of all pulses is equal, the interferogram will be a sine wave consisting of discrete points.



What happens if one pulse is more intense than the next?



When the signal is an entire emission band or bands, this effect is compounded greatly, leading to broadband noise.

Figure 6. Illustration of systematic noise introduced by source pulse instability

bands which contributed noise to the weaker band were filtered out optically, either by the use of filters or strategic selecting of detector/beamsplitter combination.

In extreme cases including very low signal, large source intensity fluctuations, and/or significant scattering of laser light into the detector, a mirror position other than the position corresponding to the zero path difference has had the highest intensity in the interferogram. The position corresponding to zero path difference should be the most intense in the interferogram since it is the only position where there is complete constructive interference of all wavelengths and is the centerburst in a typical interferogram. (85) It was necessary to fix the proper zero path difference position, as opposed to the most intense, as the centerburst, or Fourier transform errors resulted.

CHAPTER 3

EXPERIMENTAL RESULTS

This chapter contains results from absorption and emission spectra obtained from the Er:YAG, Er:LuAG, and Er:YSO samples, and a brief interpretation of the results. A more thorough discussion and examination of the data will follow in Chapter 4.

Absorption

Absorption spectra of Er:YAG (4,6,26,34,35,37,38,46), Er:LuAG (9), and Er:YSO (34,36,39,40) are well documented in the literature. These include spectra collected at both room temperature (~ 300 K) and at low (liquid helium or nitrogen) temperatures. While low temperature spectra are necessary to make individual Stark level assignments, all absorption spectra in this study were obtained at room temperature (~ 300 K), which was sufficient to identify pump frequencies for emission study and to check for any impurities or anomalies in the specific samples.

The Bruker IFS66 Spectrometer was used for all absorption measurements. Measurements were taken over two spectral regions:

"visible" (9000-25000 cm^{-1}), which utilized a quartz beamsplitter and a Si diode detector, and IR (2000-15780 cm^{-1}), which used a calcium fluoride beamsplitter and indium antimonide detector (see Figure 3). Some IR absorption spectra were also taken over the 2000-10500 cm^{-1} range. A tungsten lamp was used as the light source for all measurements. The number of scans for signal averaging ranged from 32 to 2000, and spectral resolution was typically 2 cm^{-1} .

Figure 7 contains Er:YAG absorption spectra. Although measurements were taken on several concentrations of erbium in YAG only the 2.1% concentration data is shown, since varying the concentration in a given crystal host was found by experiment to not affect the absorption bandshapes. Er:LuAG absorption spectra are shown in Figure 8. Absorption spectra for Er:YSO are shown in Figures 9-11. There are two inequivalent sites occupied by erbium in Er:YSO, and the YSO host has three principal axes of polarization (39). Unoriented absorption spectra are shown in Figure 9. Figures 10 and 11 are infrared and visible absorption spectra for light polarized parallel to the three polarization axes. All the transitions seen in Figures 7 through 11 have the ground state $^4I_{15/2}$ manifold as their initial level and terminate in the levels as indicated on the spectra. Figure 12 shows the energy level diagram containing the manifolds involved in the absorption bands in Figures 7-11. The same bands are present in Figures 10

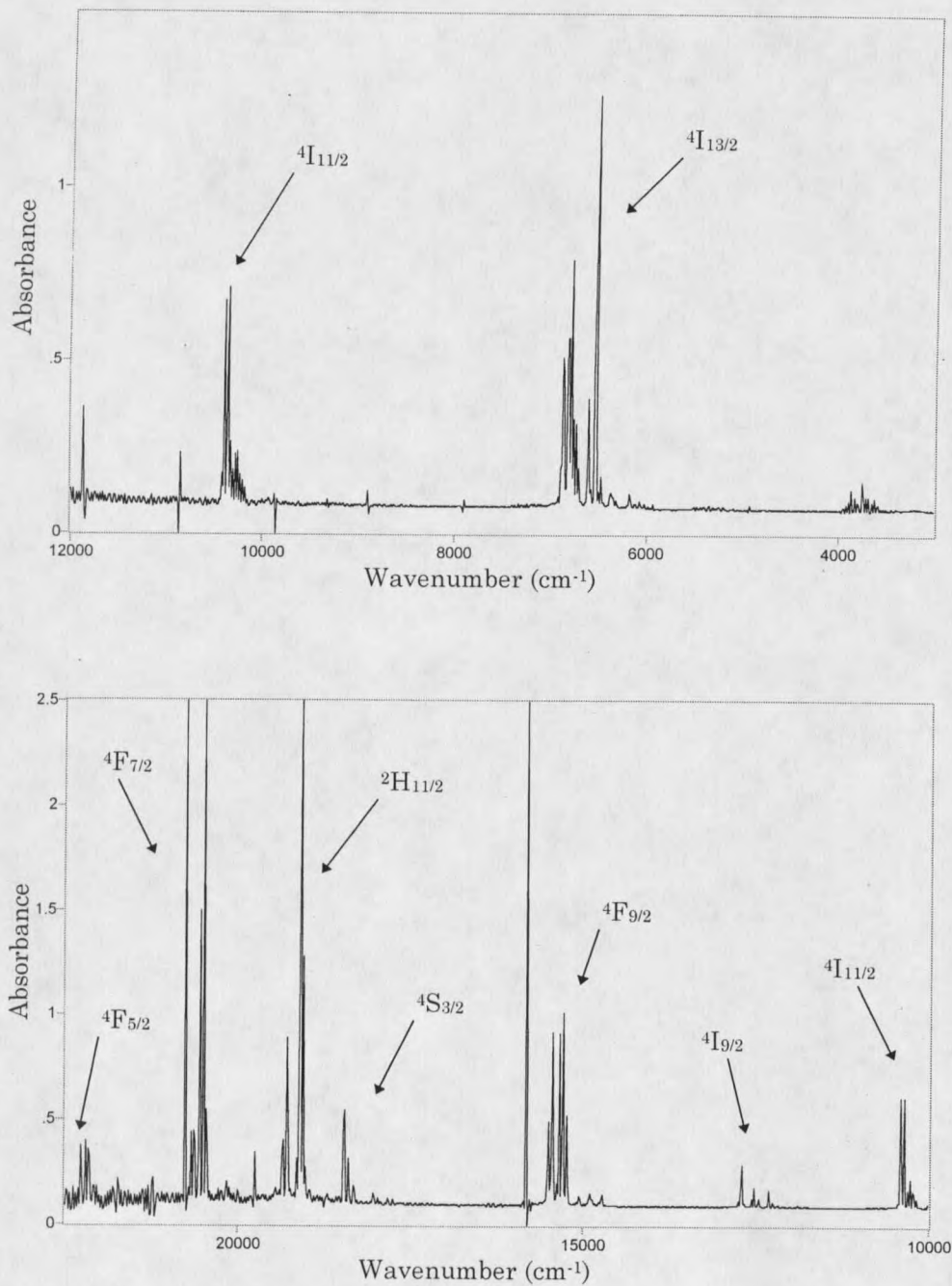


Figure 7. IR (top) and Visible Absorption Spectra of Er:YAG.

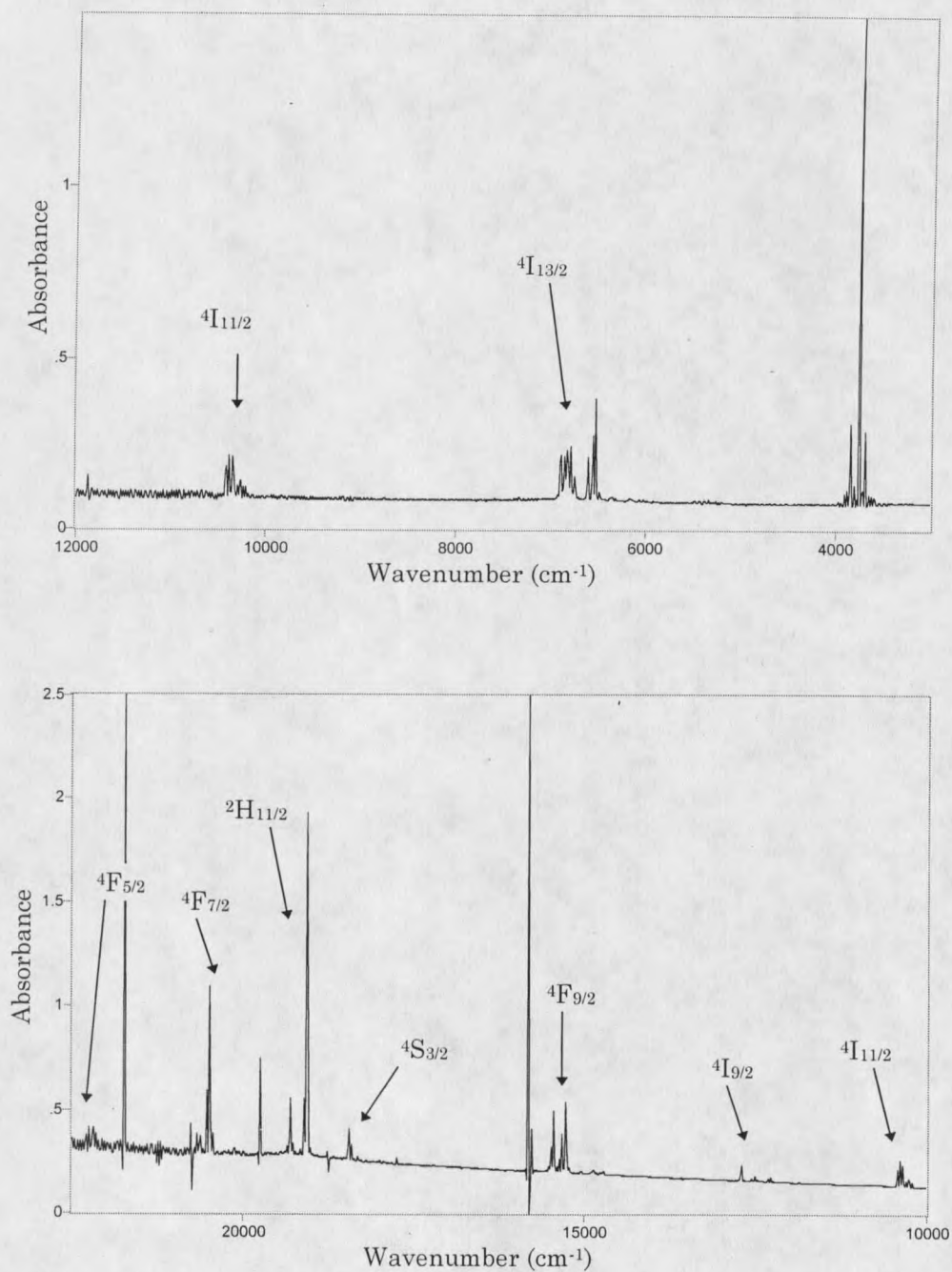


Figure 8. IR (top) and Visible Absorption Spectra of Er:LuAG.

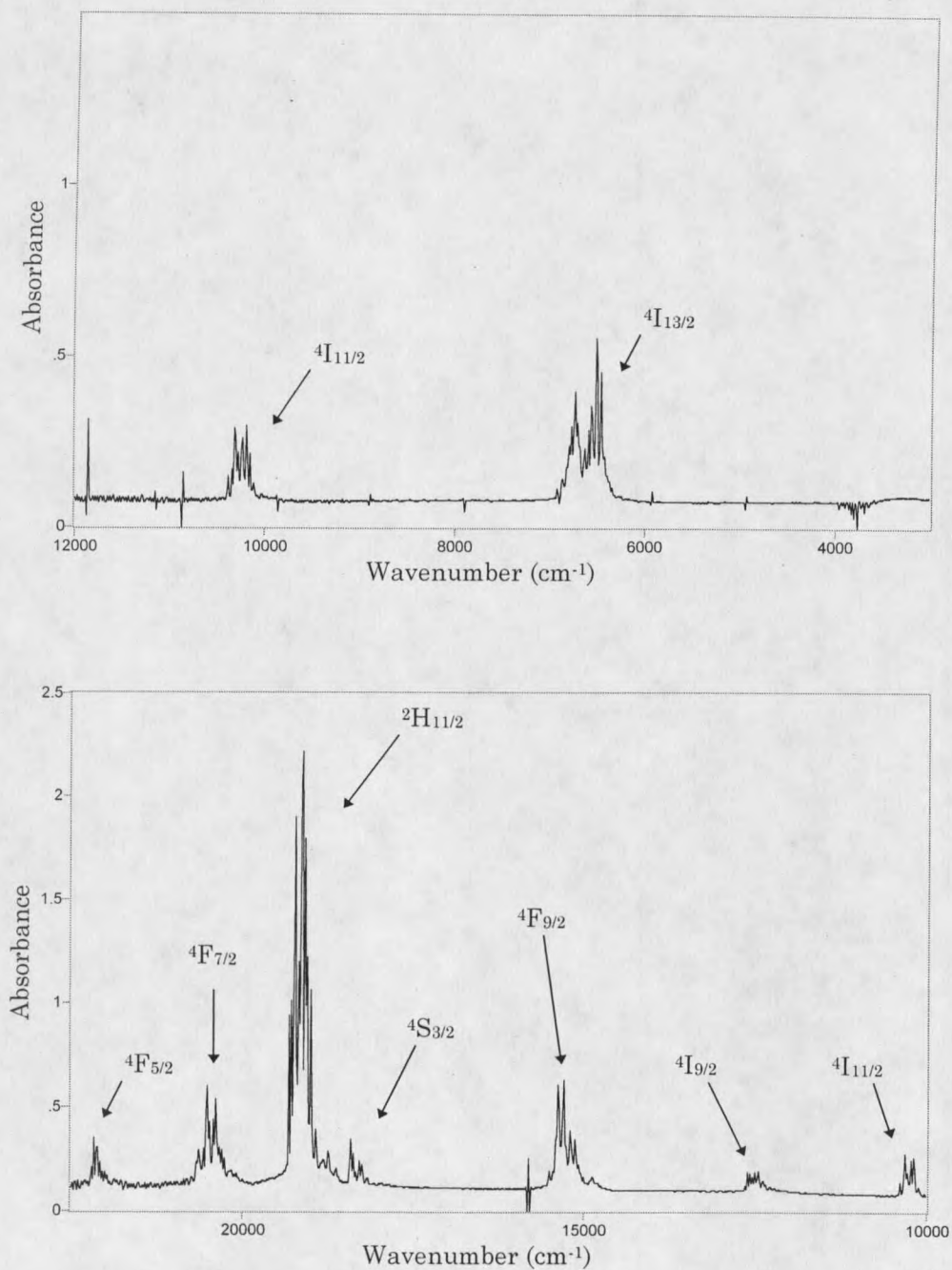


Figure 9. Unoriented IR (top) and Visible Absorption Spectra of Er:YSO.

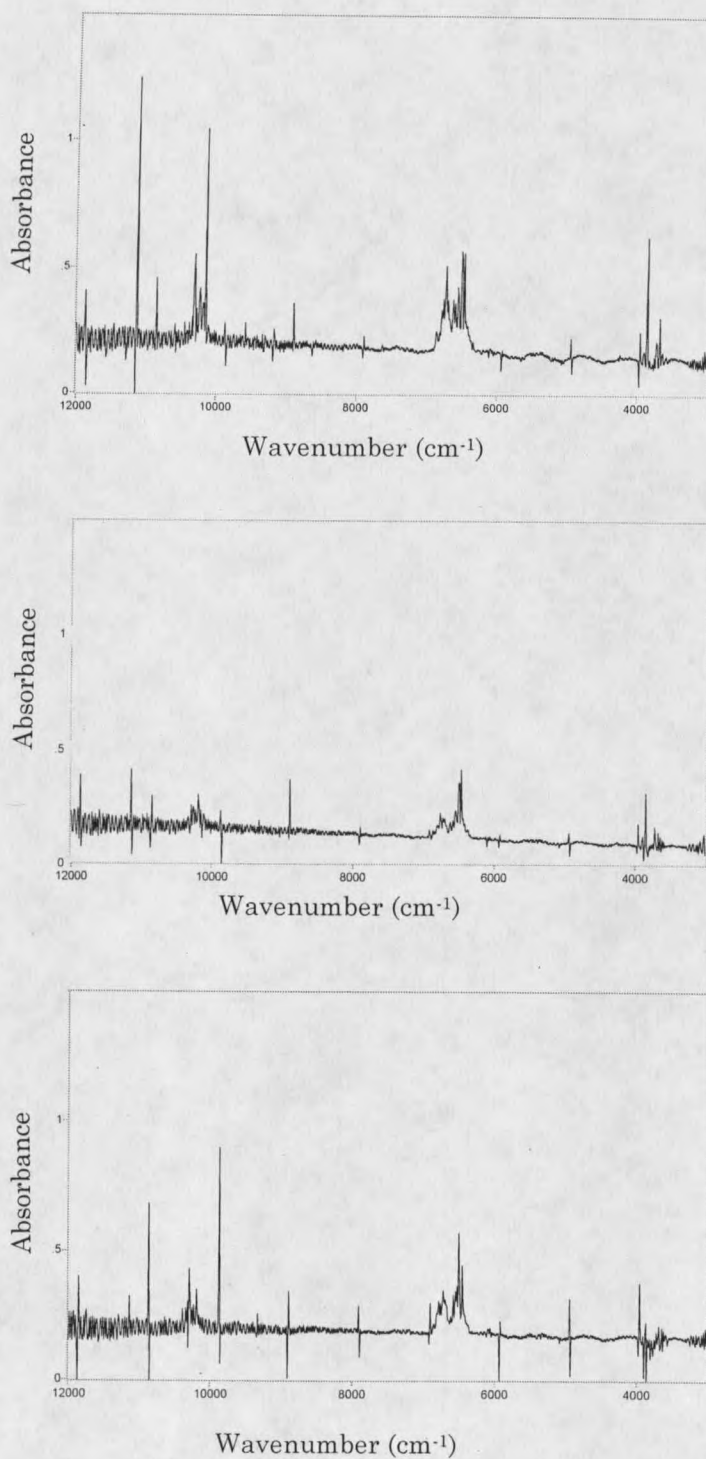


Figure 10. IR Absorption Spectra of Er:YSO for Light Polarized Parallel to the $\langle 010 \rangle$, D_1 , and D_2 Directions.

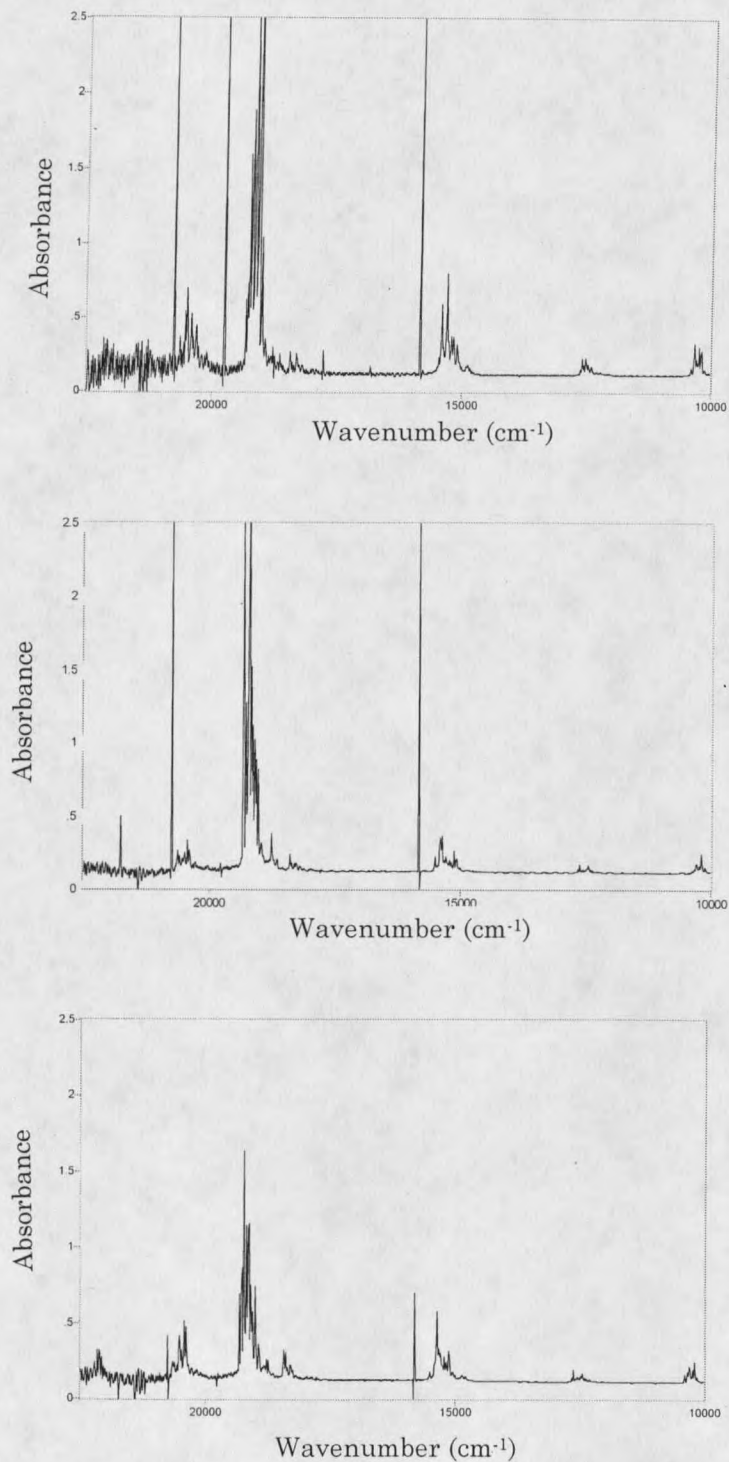


Figure 11. Visible Absorption Spectra of Er:YSO for Light Polarized Parallel to the $\langle 010 \rangle$, D_1 , and D_2 Directions.

and 11 as in Figure 9. The band just under 4000 cm^{-1} in the IR spectra is a water absorption band resulting from imperfect background correction. The sharp spikes occurring at regular wavenumber intervals (especially noticeable in Figure 10) are noise caused by interference from AC power supplies in the laboratory.

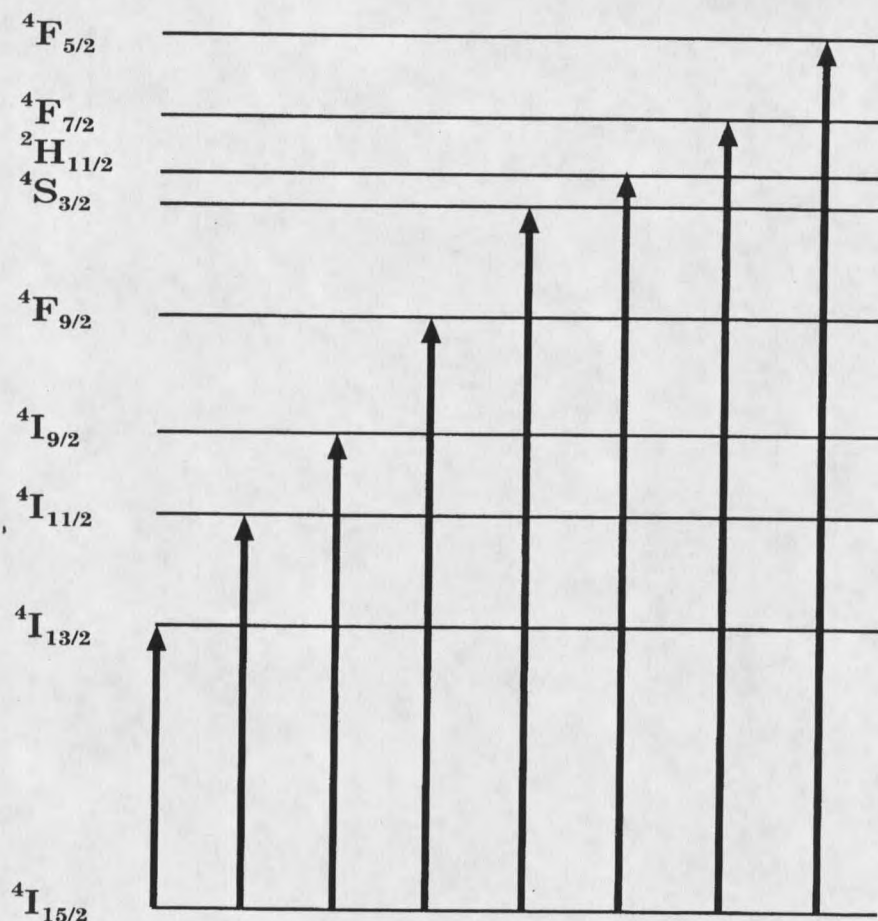


Figure 12. Absorption Transitions Observed in Figures 7-11.

Comparison of Figures 7, 8 and 9 (IR spectra of Er:YAG, Er:LuAG, and Er:YSO respectively) shows the effect of the host crystal field on the erbium

energy level structure. Examination of the spectra shows that, in general, the Er:YSO bands are about 100 cm^{-1} lower in energy than the corresponding bands in the Er:YAG and Er:LuAG spectra. More notably, for any of the transitions labeled 1 through 8 on Figure 12, the absorption bandshapes for Er:YSO are quite different than those of the erbium doped garnets. These differences are due to the crystal fields of the hosts splitting the erbium free ion levels differently, yielding a different Stark level structure in the three host materials. Since the crystal fields of the two garnet hosts are much more similar to each other than they are to YSO, the differences in the absorption spectra of Er:YAG and Er:LuAG are much more subtle.

Absorption spectra (4,6,26,34,35,37,38,46) and studies in which individual Stark levels are identified (26,37) have been performed previously in Er:YAG. Good overall agreement was seen between the measurements taken in this study and room temperature measurements in the literature (4,6,35,38). Both bandshapes and absorption band frequencies were in good general agreement. Similarly, good overall agreement was noted between the Er:LuAG absorption spectra from this study and literature data (9). Comparison of the Er:YAG and Er:LuAG spectra with data obtained in the individual energy level cold temperature studies (4,9,26,37) shows some deviations which are expected between spectra taken at room temperature and liquid helium or nitrogen temperature. First, the room temperature spectra were more congested with features. Secondly, each manifold in my

room temperature data is broadened 60 - 100 cm^{-1} over the corresponding band in the 4K data. In each case, the broadening was toward the low frequency side of the bands. This was expected since population of the upper Stark levels of the ground state $^4I_{15/2}$ manifold leads to more absorption pathways to each upper state manifold, broadening the absorption bands. The resulting new absorption pathways are lower in frequency, since they are initiated from upper Stark levels of the ground state manifold.

Analogously, good agreement was seen the orientationally resolved absorption spectra of Er:YSO (Figures 10 and 11) in this study and the room temperature data in the literature (34,36,39,40). Similar broadening of the room temperature Er:YSO spectra relative to cold temperature spectra in the literature (39) was observed. Table 3 at the end of this chapter lists individual absorption peak frequencies for the three materials studied. The peak frequencies correspond to absorptions between individual Stark levels and show reasonable agreement with those encountered in the literature. (1,4,9,26,37,39,46).

Continuous Emission

Fluorescence spectra have been obtained for Er:YSO (39), Er:YAG (4,16,37,38,46), and Er:LuAG (9) at a variety of erbium concentrations. The spectra obtained in this study were consistent with the literature

measurements. The Er:YSO emission spectra obtained in this study were not orientationally resolved along the three polarization directions. As would be expected, comparison of the polarized emission spectra of Er:YSO in the literature (39) with data obtained in this study shows features resulting from all three polarizations are present in my data.

In this study, the 488 nm line from one of two Ar-ion lasers (see Chapter 2) provided continuous excitation of erbium in both YAG and YSO to the $^4F_{7/2}$ manifold. Additionally, the Ar-ion was used to pump a cw dye laser, which, when using the laser dye DCM, provided cw excitation to the $^4F_{9/2}$ manifold. Figure 13 contains energy level diagrams illustrating the emission transitions observed after $^4F_{9/2}$ and $^4F_{7/2}$ excitation, respectively. Nonradiative relaxations are not indicated in the energy level diagrams. Continuous emission data was not obtained for Er:LuAG, though numerous temporally resolved emission spectra were obtained for this material (discussed in the next section). Visible and IR emission spectra were obtained at the same spectral ranges and using the same beamsplitters and detectors as the absorption spectra. The number of scans used for signal averaging ranged from 64 to 2000, and resolutions of either 8 or 16 cm^{-1} were obtained at room temperature. In order to compare the strength of different emission transitions in the same spectrum, it was necessary to correct for instrument response. This was accomplished by recording a response curve

using a tungsten lamp, then eliminating the lamp contribution by dividing a calculated intensity versus frequency curve for a blackbody at 3500 K.

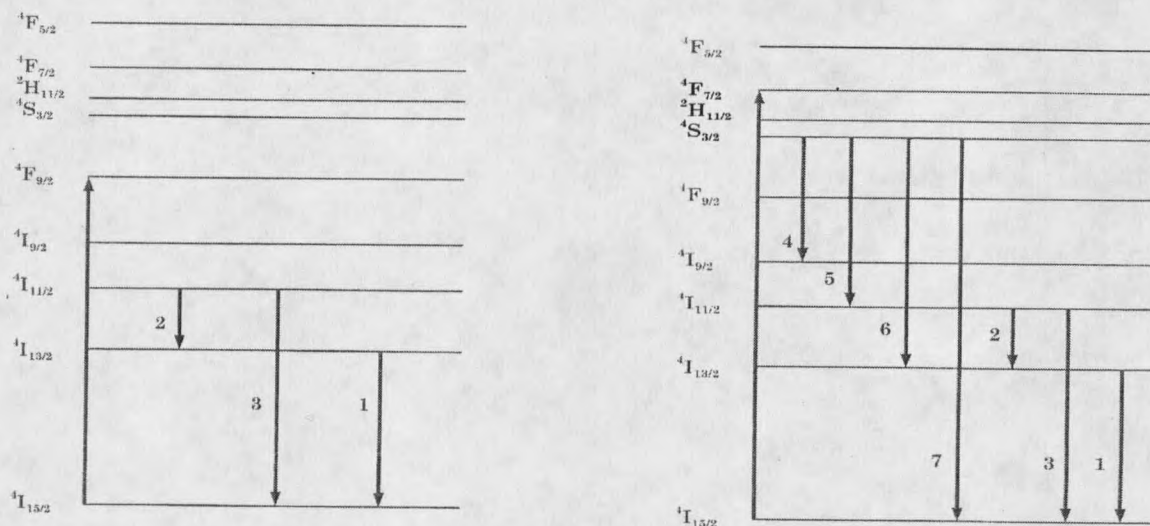


Figure 13. Radiative Emission Transitions Observed for ${}^4F_{9/2}$ and ${}^4F_{7/2}$ Excitation.

IR Emission

Figure 14 is a fluorescence spectrum of 4% Er:YAG, pumped to the ${}^4F_{9/2}$ manifold by 15446 cm^{-1} dye laser output. Assignments of the emission bands are shown on the spectra. In the bottom view, the y-axis (intensity) is scaled to enable a closer look at the two weaker transitions. The same transitions were observed in the emission spectrum of 2.1% Er:YAG. Figure 15 contains a similar spectrum of 2% Er:YSO, which was excited at a slightly lower frequency (15376 cm^{-1}) due to the different Stark level splitting of the YSO host. The transitions initiated from the ${}^4I_{11/2}$ manifold are not seen due

to the lower signal to noise ratio in this experiment. The different host

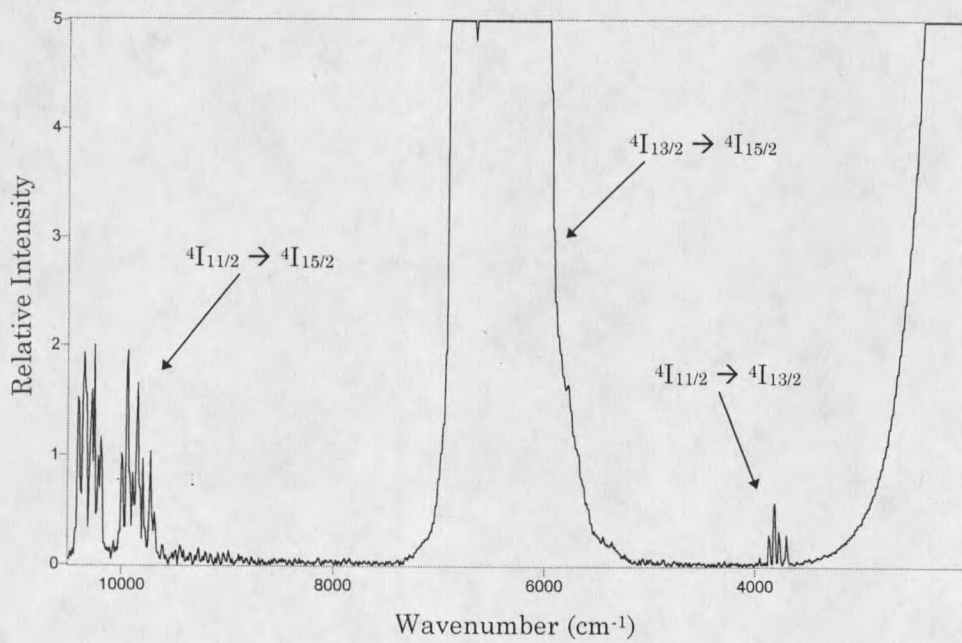
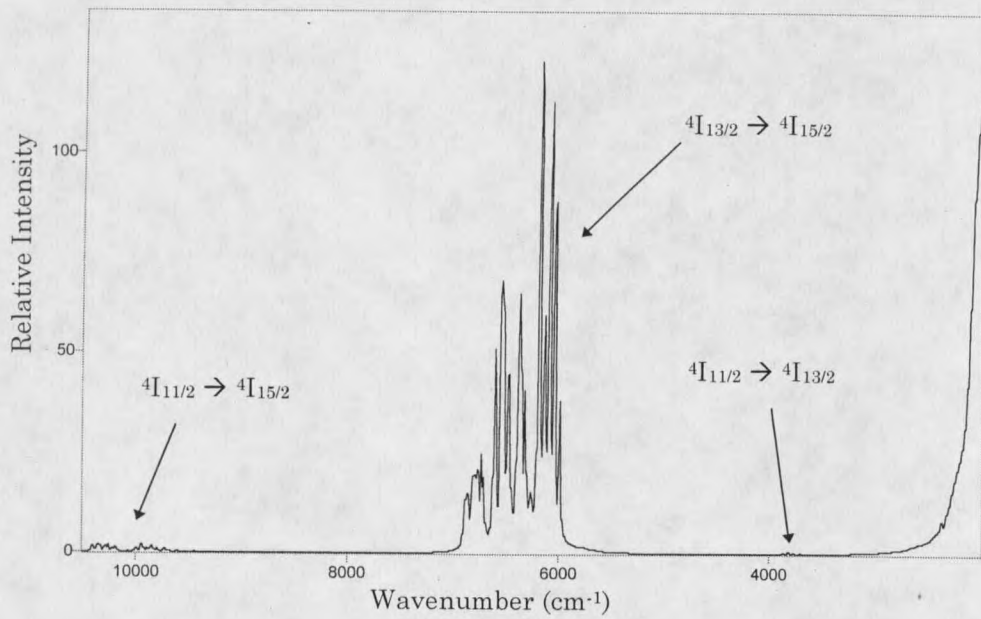


Figure 14. IR Emission Spectrum of Er:YAG Pumped to the $4F_{9/2}$ Manifold.

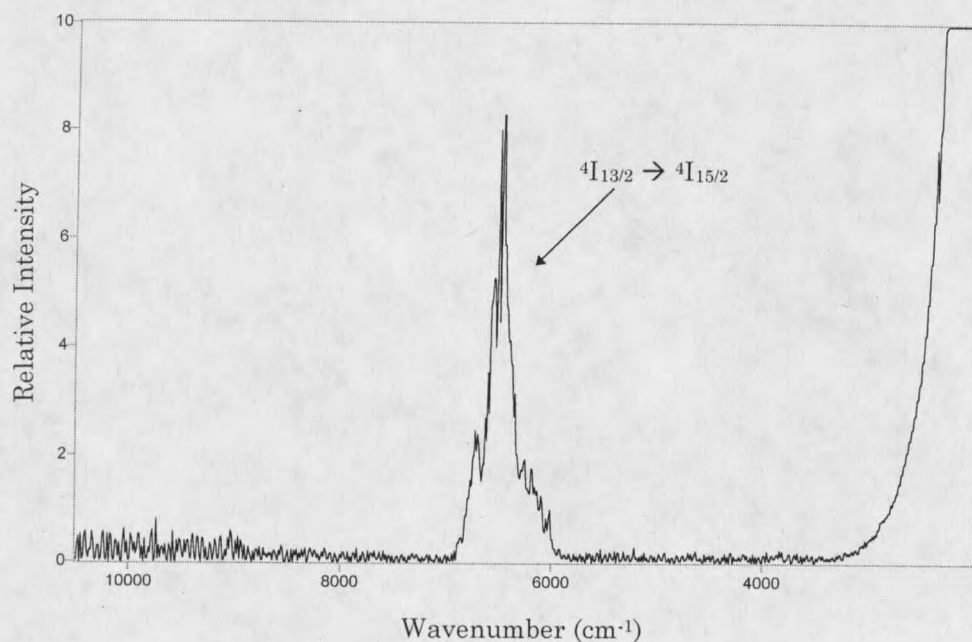


Figure 15. IR Emission Spectrum of Er:YSO pumped to the $4F_{9/2}$ Manifold.

effects also exhibit themselves in the emission spectra. The Er:YSO $4I_{13/2} \rightarrow 4I_{15/2}$ emission band does not exhibit the sharp lines seen in the Er:YAG samples. This trend generally holds for the other emission bands throughout the infrared and visible regions examined in this study. The apparent sharp rise in intensity below about 2800 cm^{-1} is not real emission, but results from imperfect correction for the instrument response curve, thereby representing the lower useful frequency limit for the emission spectra.

Figure 16 contains an emission spectrum of 4% Er:YAG excited to the $4F_{7/2}$ manifold using the 488 nm Ar-ion line. The top and bottom parts of the figure are simply the same spectrum, with the y-axis scaled differently to

allow examination of all the emission bands. Figure 17 features a similar treatment of 2% Er:YSO. Examination of Figures 14 and 16 reveals that ${}^4F_{7/2}$ excitation results in an emission transition that is not there under ${}^4F_{9/2}$ excitation. This transition, from the ${}^4S_{3/2}$ to the ${}^4I_{11/2}$ manifold, occurs at around 8000 cm^{-1} . The analogous emission transitions take place in Er:YSO, and are seen in Figure 17.

Visible Emission

Figure 18 shows visible emission spectra of 4% Er:YAG and 2% Er:YSO, respectively. The transition around 10000 cm^{-1} is the same ${}^4I_{11/2} \rightarrow {}^4I_{15/2}$ transition seen in the IR emission spectra. The strong green emission at approximately 18000 cm^{-1} is the ${}^4S_{3/2} \rightarrow {}^4I_{15/2}$ transition, and the very weak band at 15000 cm^{-1} is the ${}^4F_{9/2} \rightarrow {}^4I_{15/2}$ emission. The large spike seen just above 20000 cm^{-1} in both spectra is scattered 488 Ar-ion laser light. The lower signal-to-noise ratio above 22000 cm^{-1} is due to decreased instrument response (see Figure 2).

Temporally Resolved Emission

The temporally resolved emission measurements presented in this section were obtained using the experimental setup described in Chapter 2. The Infinity/OPO system provided nanosecond excitation pulses for all the

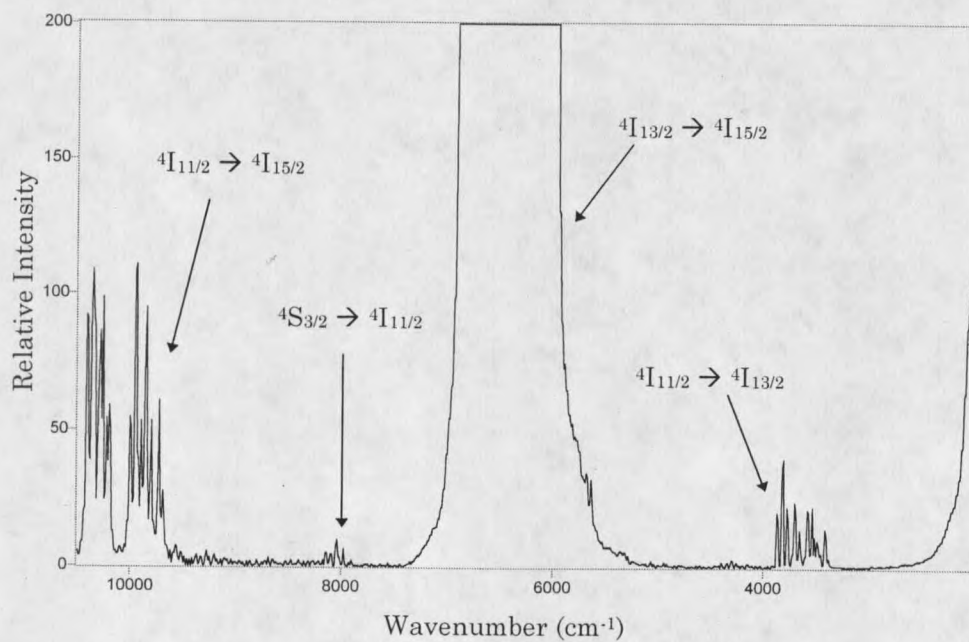
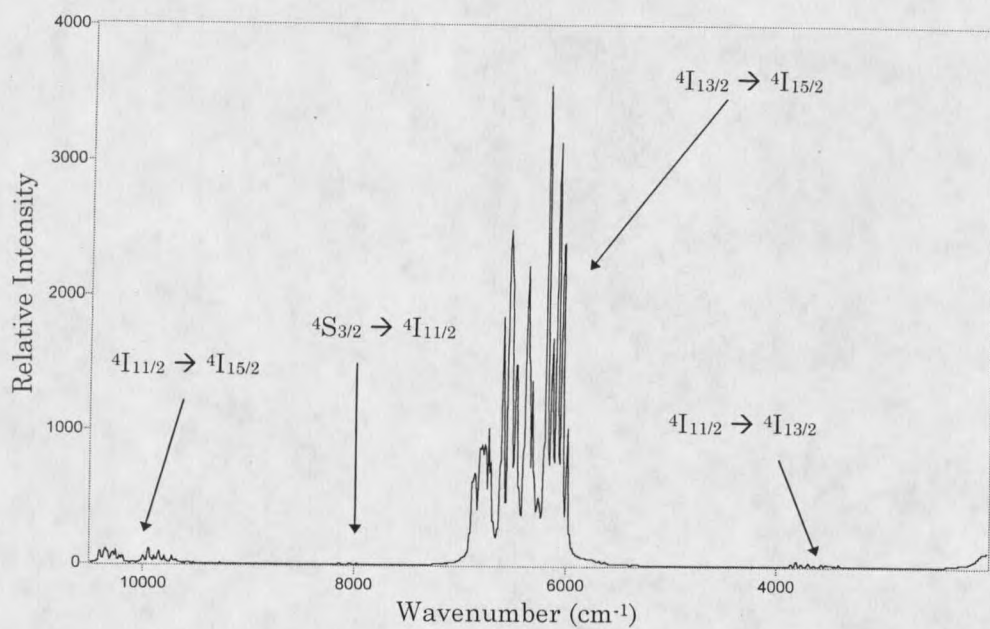


Figure 16. IR Emission Spectrum of Er:YAG Pumped to the $4F_{7/2}$ Manifold.

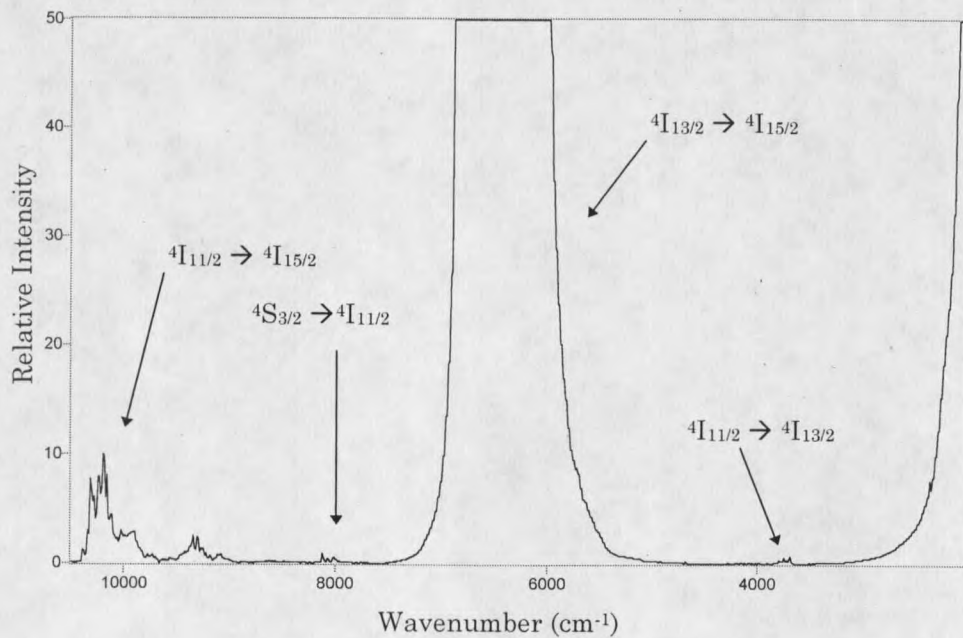
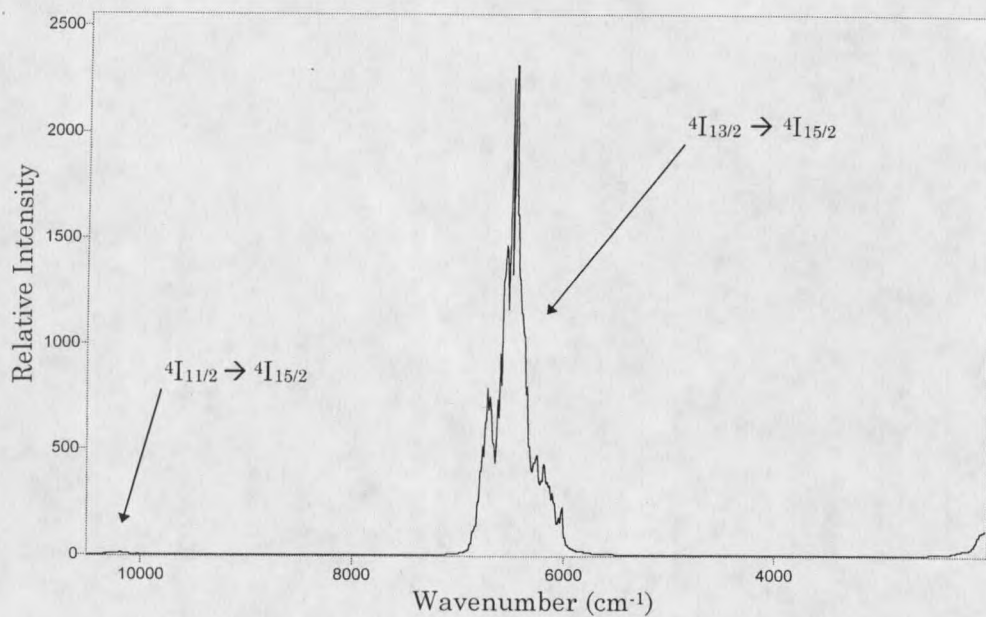


Figure 17. IR Emission Spectrum of Er:YSO Pumped to the $4F_{7/2}$ Manifold.

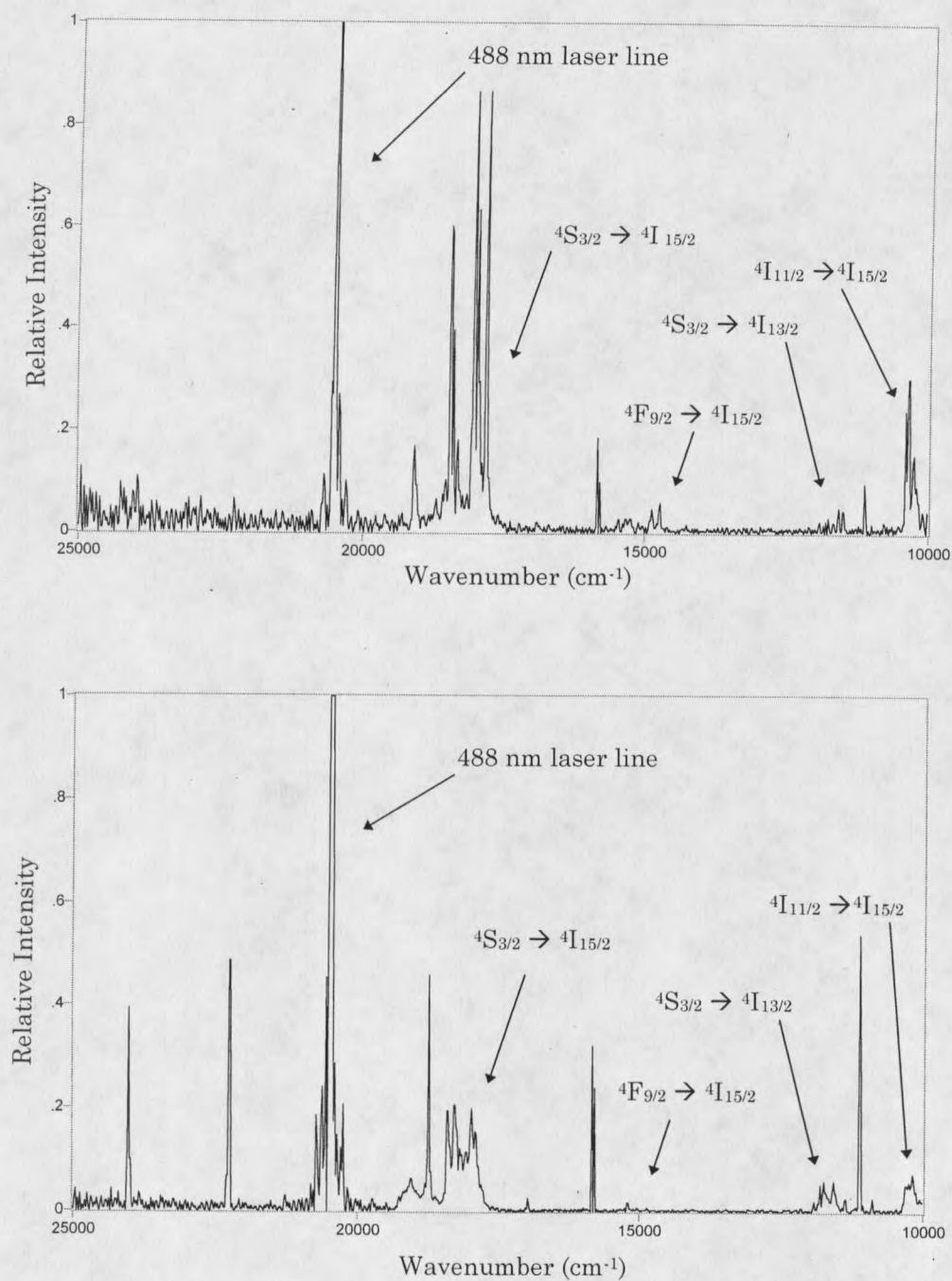


Figure 18. Visible Emission Spectra of Er:YAG (top) and Er:YSO Pumped to the $^4F_{7/2}$ Manifold.

measurements presented in this section. The spectral resolution was 16 cm^{-1} for most experiments. Unless otherwise noted, the excitation repetition rate was set at 15 Hz, which provided an interval of 66.67 ms between pulses. This repetition rate was used to allow nearly complete relaxation and corresponds to at least five exponential lifetimes for the slowest emission (${}^4\text{I}_{11/2} \rightarrow {}^4\text{I}_{15/2}$) decay. Infrared time-resolved emission was collected after excitation to each of the first eight excited state manifolds of erbium (${}^4\text{I}_{13/2}$ through ${}^4\text{F}_{5/2}$). These excitation manifolds can be seen in Figure 12.

In the following paragraphs, results which are common to all the erbium materials studied will be presented. Where applicable, examples to illustrate these results will be provided using Er:YSO emission spectra since the time resolved spectra collected for this material showed the best overall signal-to-noise. The spectra shown in this section have not been corrected for instrument response.

Selective excitation at different pump wavelengths allowed observation of the "turning on and off" of emission bands, helping to confirm the originating manifold of the emission transitions. When pumped to the ${}^4\text{I}_{13/2}$ manifold, the resulting emission spectrum (Figure 19) contains only one transition, from the ${}^4\text{I}_{13/2}$ directly back to the ground state manifold. The emission occurs on the millisecond time scale at around 6500 cm^{-1} . Each spectral "time slice" shown in Figure 19 is at a 250 microsecond interval.

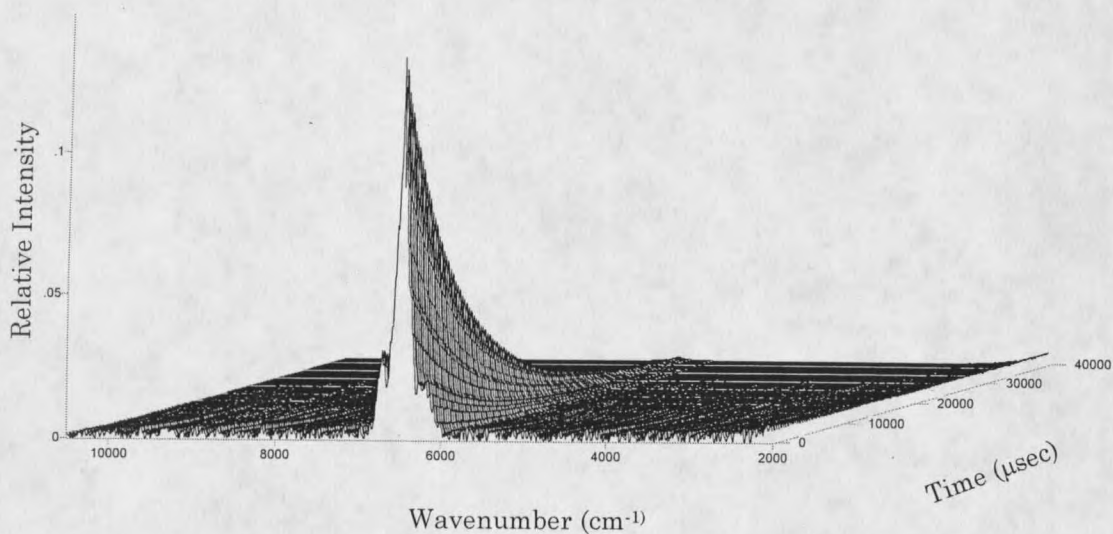


Figure 19. Temporally Resolved Emission of Er:YSO Following Excitation to the ${}^4I_{13/2}$ Manifold.

Excitation to any of the next three higher manifolds (${}^4I_{11/2}$, ${}^4I_{9/2}$, or ${}^4F_{9/2}$) yields two additional emission transitions, originating from the ${}^4I_{11/2}$ manifold and terminating in the ${}^4I_{13/2}$ and ${}^4I_{15/2}$ manifolds, resulting in an emission spectrum as seen in Figure 20. These two new emissions decay on a considerably faster time scale than the ${}^4I_{13/2} \rightarrow {}^4I_{15/2}$ transition shown in the previous spectrum. The ${}^4I_{13/2} \rightarrow {}^4I_{15/2}$ transition is still present at 6500 cm^{-1} , but is still rising in intensity on the faster time scale of Figure 20, where each time slice is five microseconds. The fact that the two new emissions decay on the same time scale indicates that their emitting levels are depopulated on the same time scale, so they almost certainly originate from the same manifold. This illustrates one benefit of the temporally resolved method, that it helps in assignment of the emission transitions.

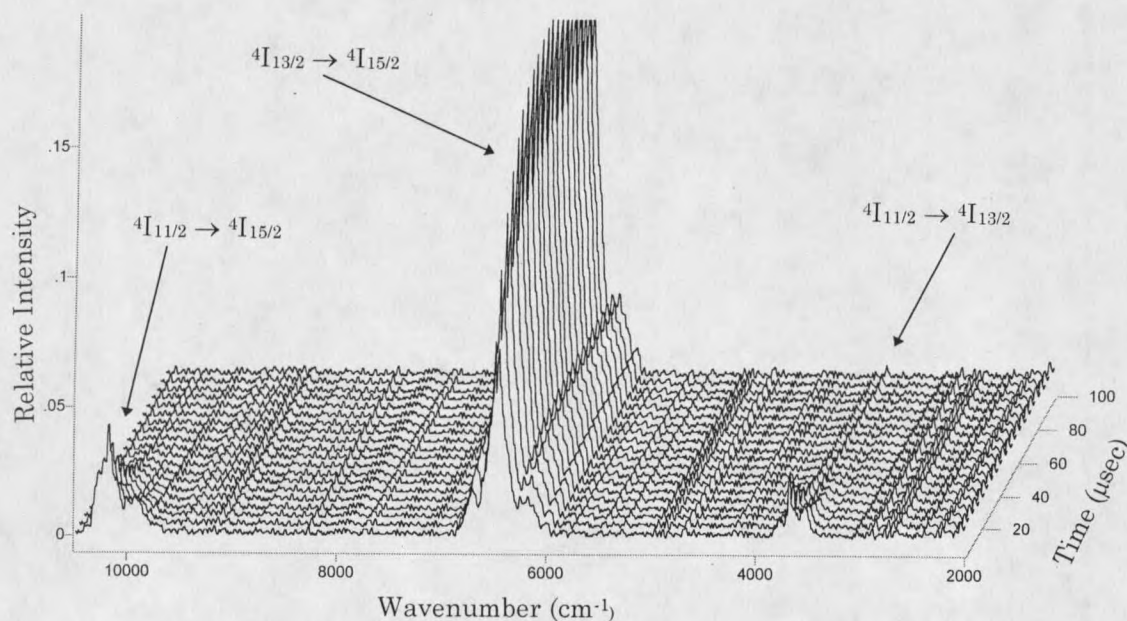


Figure 20. Temporally Resolved Emission of Er:YSO Following Excitation to the ${}^4I_{11/2}$ Manifold.

Pumping at or above the ${}^4S_{3/2}$ manifold yields three additional emission bands, as can be seen in Figure 21. These three bands also occur on the microsecond time scale, but decay even faster than the emissions from the ${}^4I_{11/2}$ manifold. These three bands, occurring at roughly 5800, 8000, and 11500 cm^{-1} , originate from the ${}^4S_{3/2}$ manifold and terminate in the ${}^4I_{9/2}$, ${}^4I_{11/2}$, and ${}^4I_{13/2}$ manifolds, respectively. Additionally, an emission band at approximately 18000 cm^{-1} (${}^4S_{3/2} \rightarrow {}^4I_{15/2}$, Figure 13) can be seen in the visible spectrum. Figure 21 illustrates another benefit of the temporally resolved emission method. In a time resolved experiment with temporal resolution of 5 microseconds or higher, the ${}^4S_{3/2} \rightarrow {}^4I_{9/2}$ transition will be detected at 5800

cm^{-1} . However, in continuous spectra such as Figure 17, this emission band is hidden by the strong, long-lived ${}^4\text{I}_{13/2} \rightarrow {}^4\text{I}_{15/2}$ band. The time resolved technique enables deconvolution of emission bands that overlap spectrally but have different temporal behavior.

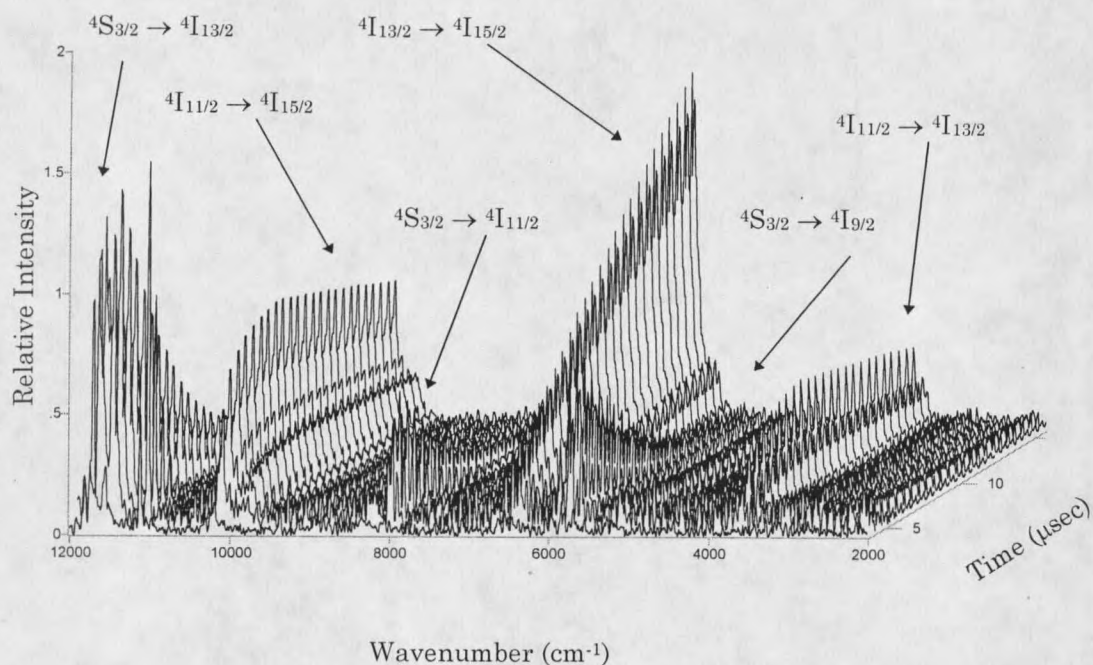


Figure 21. Temporally Resolved Emission of Er:YSO Following Excitation to the ${}^4\text{F}_{7/2}$ Manifold. The collected data set includes time from 0-130 μsec , but the data is truncated for visual clarity.

The weak emission from the ${}^4\text{F}_{9/2}$ manifold to the ground state was not observed in the time resolved spectra due to its short lifetime and low signal-to-noise ratio. In the following sections, specific results for the three materials studied are presented.

Er:YSO

The 2% Er:YSO sample was excited at the various frequencies as listed in Table 1. At each excitation frequency, experiments were run at the necessary temporal resolutions and sampling times to capture the temporal behavior of all the emission bands that occurred for a particular excitation.

Table 1. Excitation Frequencies for 2% Er:YSO.

Pump Manifold	Excitation Frequency (cm ⁻¹)
⁴ I _{13/2}	6508
⁴ I _{11/2}	10195
⁴ I _{9/2}	12606
⁴ F _{9/2}	15376
⁴ S _{3/2}	18409
² H _{11/2}	19223
⁴ F _{7/2}	20494
⁴ F _{5/2}	22095

Although there are two different Er³⁺ sites in Er:YSO, Li, Wyon, and Moncorge (39) have shown that they can be considered together in the analysis of fluorescence dynamics, since excitation of the two different sites to different degrees resulted in the same emission lineshapes (see pg. 14). Therefore, polarized temporally resolved emission spectra were not obtained in this study. In the following paragraphs, results for each of the emission transitions when pumped at the different levels will be presented.

The ⁴I_{13/2}→⁴I_{15/2} emission was detected at all pump levels. Experiments run to characterize this transition had temporal resolution of 250 μsec, and data was obtained for 66.5 msec, nearly the entire time

between laser pulses given the 15 Hz repetition rate. Signal averaging was five or ten coadditions, meaning five or ten decay events were averaged at each mirror position. Figure 22 contains two plots: a "decay trace", in which the integrated area under the transition (corrected for baseline noise) for a time slice is plotted versus time, and a "log plot", in which the logarithm of the integrated transition area is plotted instead. The integration and baseline correction methods are discussed in detail in Chapter 4. In the plots shown, most of the decay traces have been normalized to a maximum intensity value of one to facilitate comparison between different spectra. The data shown in Figure 22 were obtained by after excitation directly into the ${}^4I_{13/2}$ manifold. Though valuable information concerning relaxation processes can be obtained by pumping above the upper emitting level, it is best to excite the emitting level directly when determining lifetimes to prevent emission level feeding processes from influencing lifetime measurement. The straight line of the log plot shows that the decay is exponential. An exponential fit of the decay data results in an experimentally determined lifetime of 8.6 msec (experimental lifetimes for all the materials studied are summarized in Table 4 at the end of this chapter). The data in this plot are truncated after the signal has gone below the noise level.

Two emissions originating from the ${}^4I_{11/2}$ level appear in spectra where the ${}^4I_{11/2}$ manifold or higher is pumped, terminating at ${}^4I_{13/2}$ (emission band at approximately 3500 cm^{-1}) and ${}^4I_{15/2}$ (approximately 10000 cm^{-1}). Emission

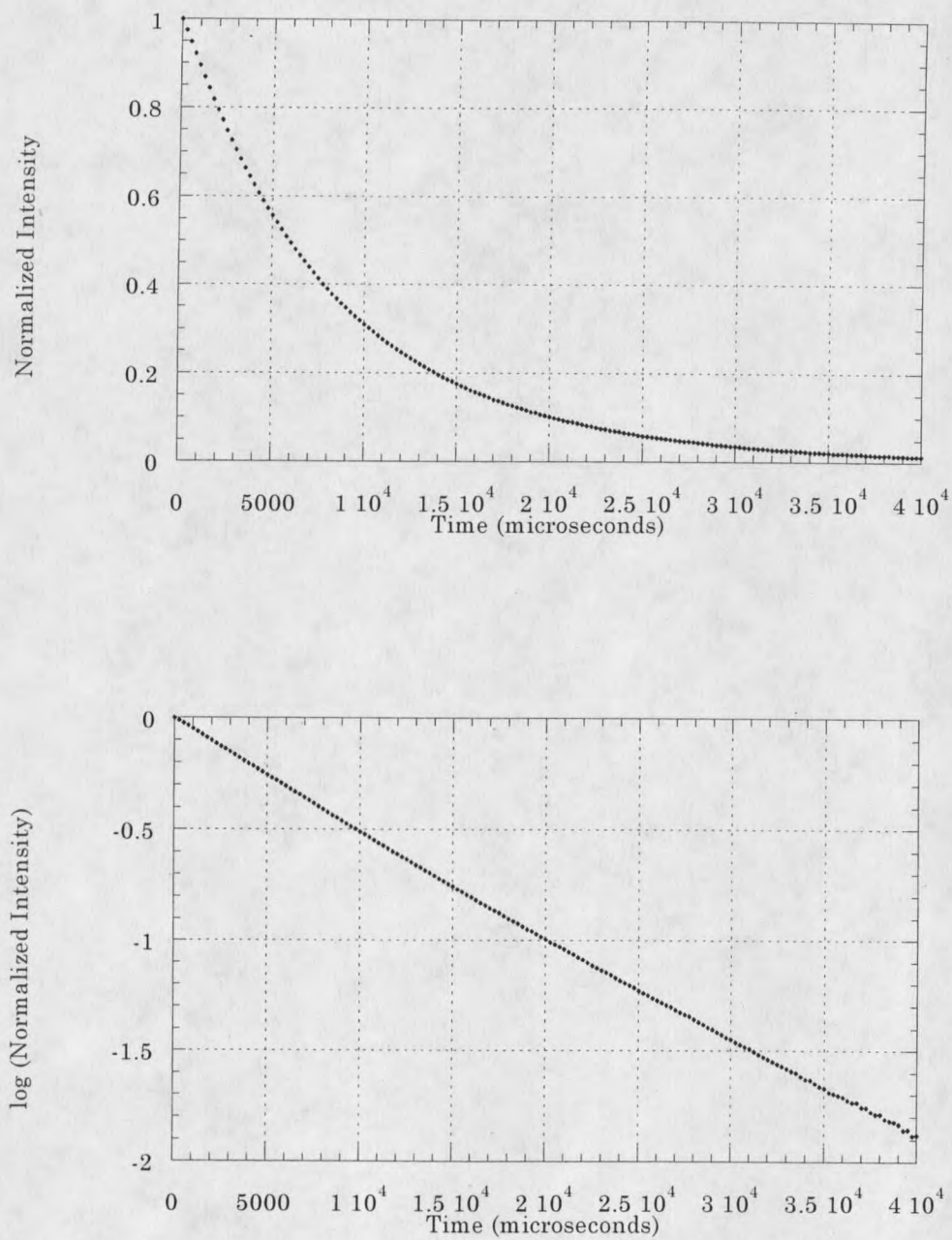


Figure 22. Decay (top) and Log of Intensity for the ${}^4I_{13/2} \rightarrow {}^4I_{15/2}$ Transition in 2% Er:YSO.

from the ${}^4I_{11/2}$ manifold has a significantly shorter lifetime than that originating from ${}^4I_{13/2}$, and the experiments designed to analyze these emission bands were temporally resolved to 500 nanoseconds and had total sampling times of 120-150 microseconds. Since this higher temporal resolution required the use of a faster, 8-bit transient recorder rather than the 16-bit recorder used for the slower experiments, lower signal-to-noise resulted, necessitating more coadditions (20 to 80 for the various pump levels) for signal averaging. Figure 23 illustrates decay traces for the two emission bands. The maximum intensity for both bands is normalized to one to show the similar behavior of the two bands, which indicates that they originate from the same manifold. Experimentally determined lifetimes for the ${}^4I_{11/2}$ level of 2% Er:YSO ranged from 10.3 to 12.7 microseconds for all the pump levels analyzed, with values of 10.3 to 10.7 μs for experiments run with direct ${}^4I_{11/2}$ excitation. The intensity of the transition terminating in the ground state is significantly higher than that terminating in the ${}^4I_{13/2}$ level. The radiative branching ratio was determined by taking a single time slice from the experiment (an acceptable assumption since the emission bandshapes did not change over time), correcting for instrument response, and integrating the area of each emission band. The resulting branching ratio was found to be 0.91 for the ${}^4I_{11/2} \rightarrow {}^4I_{15/2}$ transition and 0.09 for ${}^4I_{11/2} \rightarrow {}^4I_{13/2}$. Branching ratio calculations for all the materials studied are summarized in Table 5 at the end of this chapter.

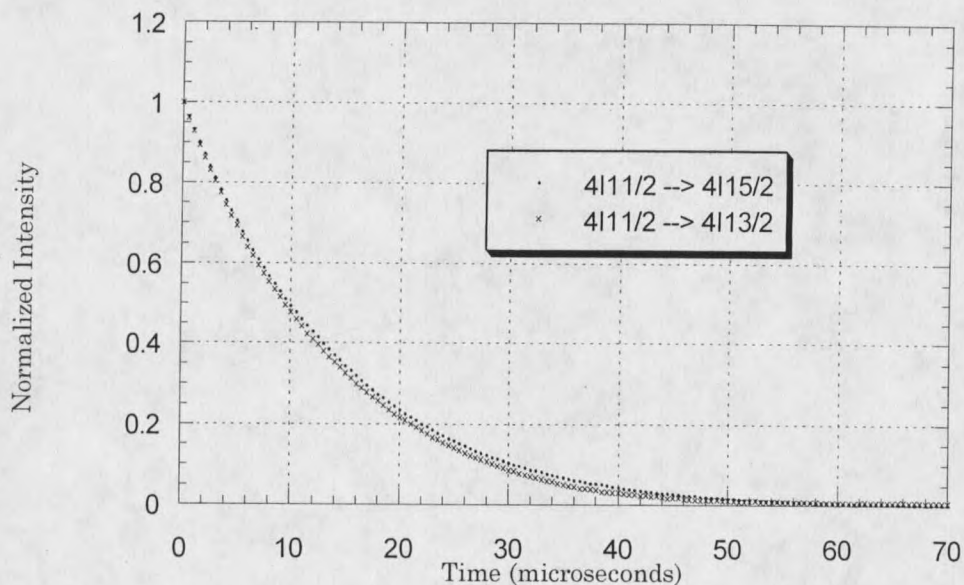


Figure 23. Decay of Emission Transitions Originating from the $4I_{11/2}$ Manifold in 2% Er:YSO.

The log plots of the above emission transitions (Figure 24) illustrate that the decays are primarily exponential. The mild degree of curvature observed in Figure 24 occurred frequently in this study and was found to be error introduced by baseline correction. The reasoning for this is discussed in the next chapter. Data points are truncated after the signal reaches the noise level.

Emission transitions originating from the $4S_{3/2}$ manifold occur when the Er:YSO was subjected to excitation to that level or higher. Spectra obtained for Er:YSO included the four emission bands originating from the

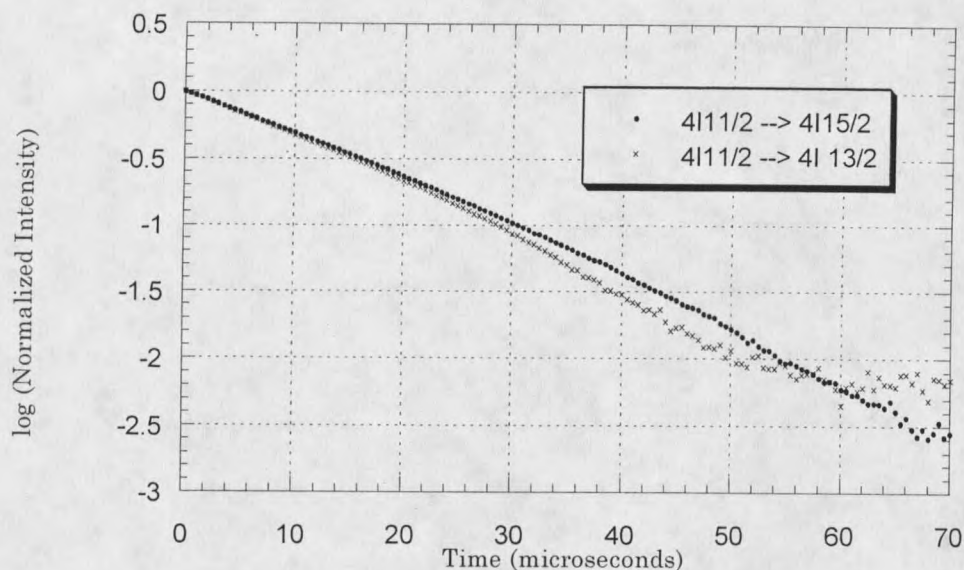


Figure 24. Log of Intensity of Emission Transitions Originating from the $4I_{11/2}$ Manifold in 2% Er:YSO.

$4S_{3/2}$ manifold that were discussed earlier in this section. Emission spectra obtained to study these transitions typically required temporal resolution of 50 nanoseconds with 400 time slices (for a total sampling duration of 20 microseconds) and 20 - 80 coadditions for signal averaging.

The IFS 66 spectrometer cannot perform time resolved experiments on both sides of the HeNe reference frequency (15798 cm^{-1}) simultaneously. The HeNe provides the reference points for where the sampling (data acquisition) is performed. Signal at higher frequencies than the HeNe are undersampled in step scan and would alias if light frequencies on both sides were detected. In continuous scan, a phase

locked loop can interpolate the HeNe curve to allow more frequent sampling which eliminates this problem. In step scan, two laser detectors are used: one to lock on a HeNe zero crossing; the other ($\sim 90^\circ$ out of phase) is used to determine the slope to tell which half wavelength is being locked on. Therefore, the strategy used in continuous scan cannot be used in step scan, and the four emission transitions originating from $^4S_{3/2}$ could not be evaluated in the same experiment. The three lower frequency transitions were observed in spectra obtained over the range of 2000 - 15700 cm^{-1} , and the visible transition (around 18000 cm^{-1}) was obtained in a separate experiment. IR spectra were obtained after excitation to the $^4S_{3/2}$, $^4F_{7/2}$, and $^4F_{5/2}$ levels. Since the silicon diode detector was easily saturated it was very difficult to detect emission transitions in the spectral region close to the excitation source, therefore, we were not able to obtain a time resolved emission spectrum containing the $^4S_{3/2} \rightarrow ^4I_{15/2}$ transition after pumping the $^4S_{3/2}$ manifold. However, this transition was observed in temporally resolved spectra after excitation to the $^4F_{7/2}$, and $^4F_{5/2}$ manifolds. Figure 25 shows decay traces of the three IR emission bands following $^4S_{3/2}$ excitation. The $^4S_{3/2} \rightarrow ^4I_{13/2}$ transition has the best signal-to-noise ratio, and an exponential fit based on this transition yields a lifetime of 3.5 microseconds. The $^4S_{3/2} \rightarrow ^4I_{11/2}$ transition is the weakest and the figure illustrates the effect of the lower signal-to-noise on the decay trace. Figure 25 also contains a log plot of the decays. Again, the slight curvature in the log traces is attributable to

baseline correction. Branching ratios were calculated for these radiative transitions based on spectra obtained after ${}^4F_{7/2}$ excitation, since a visible spectrum was obtained at that excitation level.

Er:YAG

The 4% Er:YAG sample was excited at the frequencies as listed in Table 2. Additionally, emission spectra were obtained from 2.1% Er:YAG following excitation to the ${}^4F_{9/2}$ manifold. The same emission transitions were observed for the same pump manifolds as in Er:YSO. Results for the fluorescence decays for the ${}^4I_{13/2}$, ${}^4I_{11/2}$, and ${}^4S_{3/2}$ levels are discussed in the following paragraphs.

The ${}^4I_{13/2} \rightarrow {}^4I_{15/2}$ emission occurred on a similar time scale in Er:YSO and Er:YAG, and experiments run to evaluate this transition were set up with similar temporal resolution, sampling duration, and number of coadditions. Figure 26 shows the integrated results of the transition after

Table 2. Excitation Frequencies for 4% Er:YAG.

Pump Manifold	Excitation Frequency (cm^{-1})
${}^4I_{13/2}$	6797
${}^4I_{11/2}$	10347
${}^4F_{9/2}$	15445
${}^4S_{3/2}$	18797
${}^4F_{7/2}$	20494

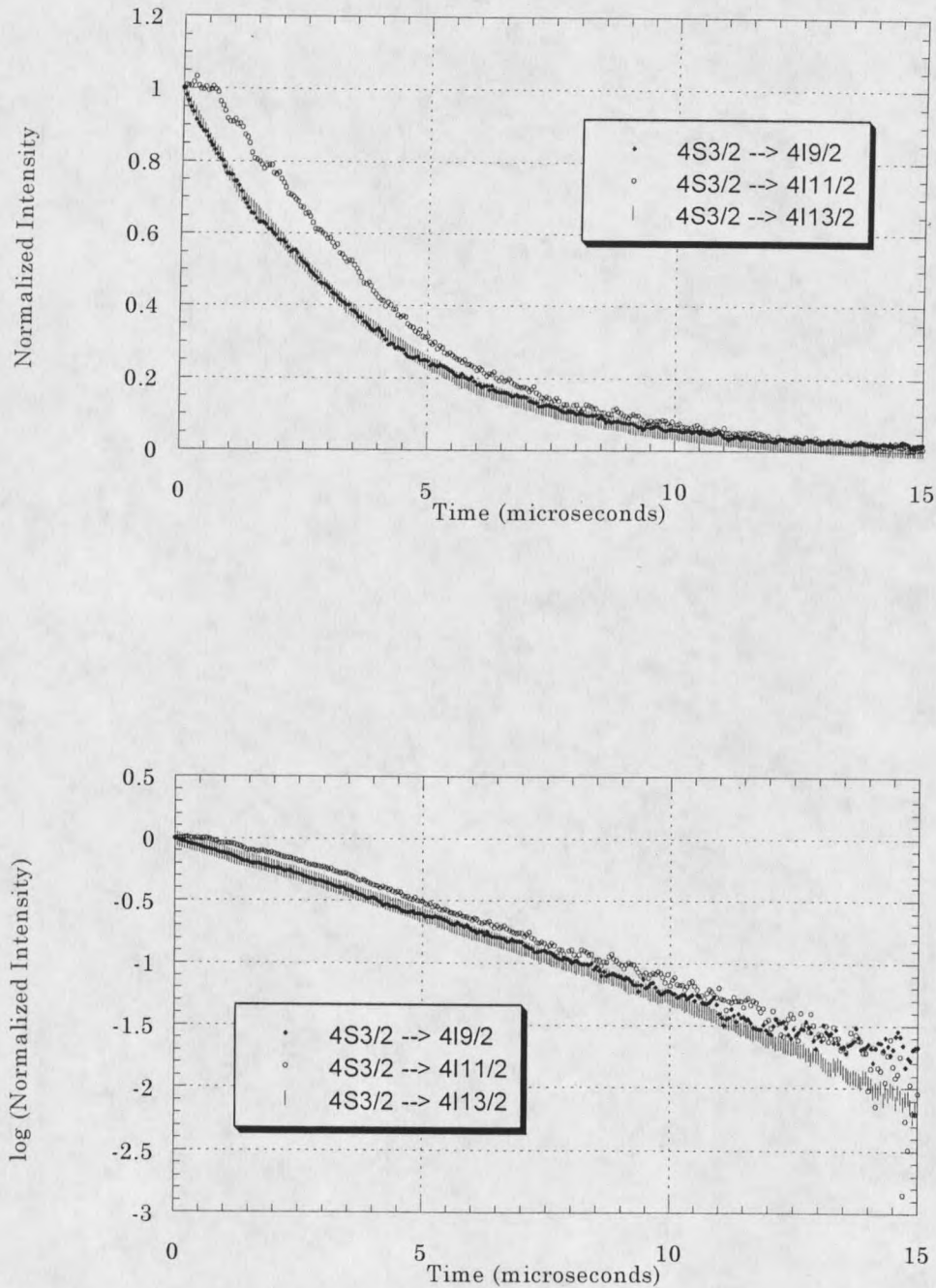


Figure 25. Decay (top) and Log of Intensity of Emission Transitions Originating from the $4S_{3/2}$ Manifold in 2% Er:YSO.

$^4F_{9/2}$ excitation for the two erbium concentrations studied. The decay profile for this transition in Er:YAG is similar regardless of excitation manifold since the emission rise time is 2-3 orders of magnitude shorter than the decay time for all the excitation levels studied.

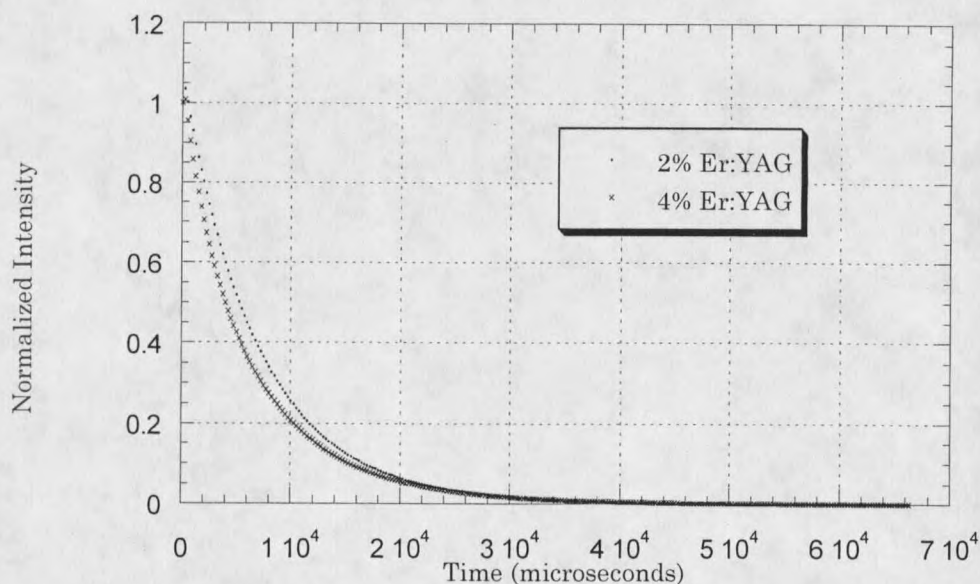


Figure 26. Decay of the $^4I_{13/2} \rightarrow ^4I_{15/2}$ Transition for 2.1% and 4% Er:YAG.

The experimentally determined lifetimes for this transition is on the order of 6.5 - 7 milliseconds for the two samples. A difference in lifetime for the two concentrations could not be confirmed within experimental error. While the traces shown in Figure 26 would seem to indicate a shorter lifetime in the 4% sample, in another similar set of experiments the decay rate was slightly faster in the 2.1% sample. Figure 27 illustrates log plots for the

decay traces shown in Figure 26. The slight curvature seen in the log plots again is attributable to baseline correction.

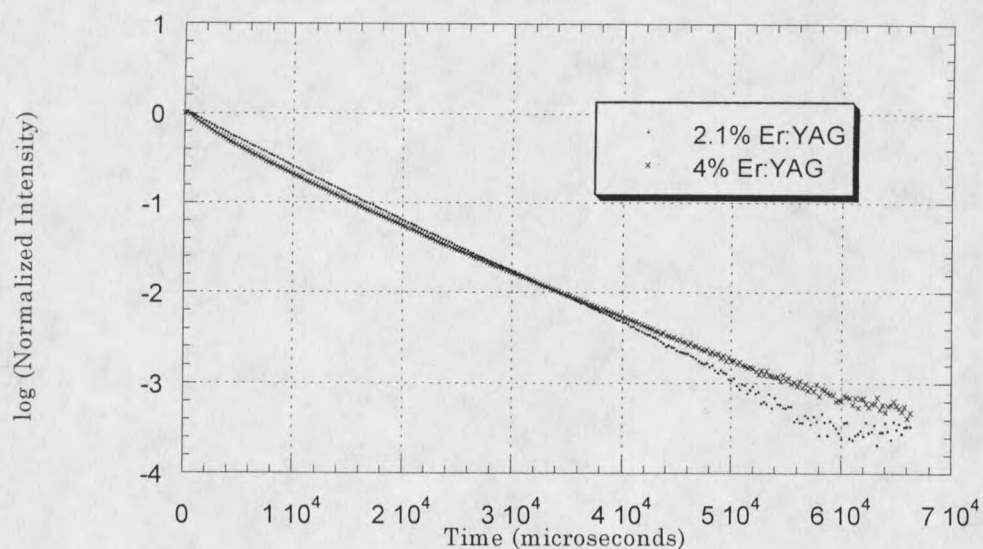


Figure 27. Log of Intensity of the ${}^4I_{13/2} \rightarrow {}^4I_{15/2}$ Emission Transition in 2.1% and 4% Er:YAG.

The two emission transitions originating from the ${}^4I_{11/2}$ manifold decay more slowly in Er:YAG than in Er:YSO. Experiments run to evaluate these transitions were typically had 1 msec temporal resolution and 500 msec total sampling time. All other experimental parameters were similar to those for the Er:YSO experiments. Figure 28 shows the integrated transition data and log plot of the fluorescence after ${}^4I_{11/2}$ excitation. The calculated lifetime is 67.3 microseconds based on the higher intensity ${}^4I_{11/2} \rightarrow {}^4I_{15/2}$ emission, with the weaker ${}^4I_{11/2} \rightarrow {}^4I_{13/2}$ emission showing good agreement. The emission

lifetime is several times longer than that of the same transition in Er:YSO. In both materials, multiphonon relaxations dominate relaxation from the $^4I_{11/2}$ level, and the mechanism appears to be more efficient in Er:YSO. Decay results for 2.1% Er:YAG were not obtained for excitation to this manifold, but experiments run on both concentrations with $^4F_{9/2}$ excitation do not show a strong concentration dependence in the 2-4% concentration range.

Figure 29 illustrates integrated transition data and a log trace of the visible $^4S_{3/2} \rightarrow ^4I_{15/2}$ emission. Decay from this level is also exponential, as shown by the log trace. The IR transitions from the $^4S_{3/2}$ level show similar temporal behavior. An exponential fit of this decay process for 4% Er:YAG yields a calculated lifetime of 10.7 microseconds, which is longer than the analogous process in Er:YSO (approximately 3.5 microseconds). The temporal resolution for the experiments run to analyze these transitions was 250 nsec, with a total sampling time of 150 microseconds. Other experimental parameters were the same as those for the Er:YSO experiments.

Er:LuAG

Time resolved emission spectra were obtained for 0.5% Er:LuAG after excitation to the $^4I_{13/2}$, $^4I_{11/2}$, and $^4S_{3/2}$ manifolds, using pump energies of 6525, 10385, and 18448 cm^{-1} , respectively. As with the other samples, the pump manifolds were selected since they are the emitting levels. The same

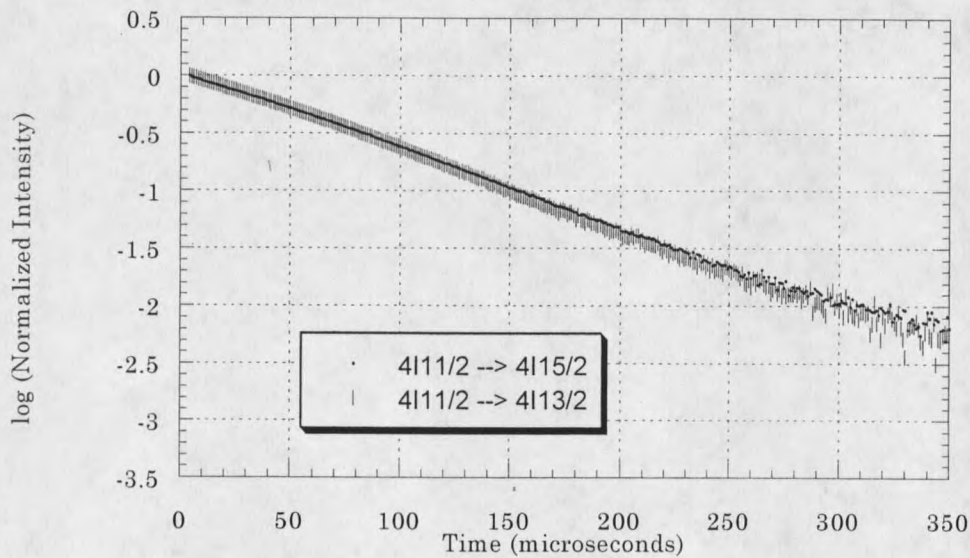
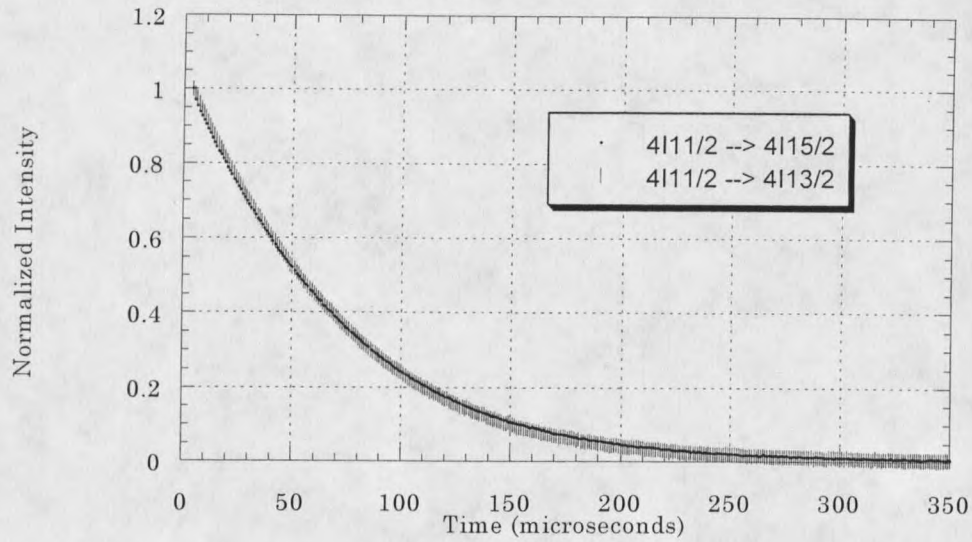


Figure 28. Decay (top) and Log of Intensity of Emission Transitions Originating from the $4I_{11/2}$ Manifold in 4% Er:YAG.

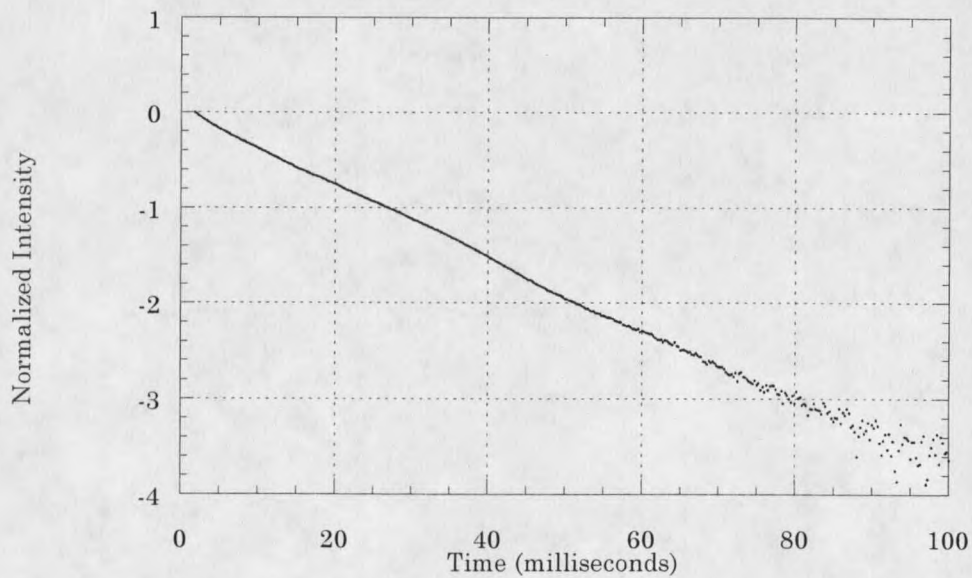
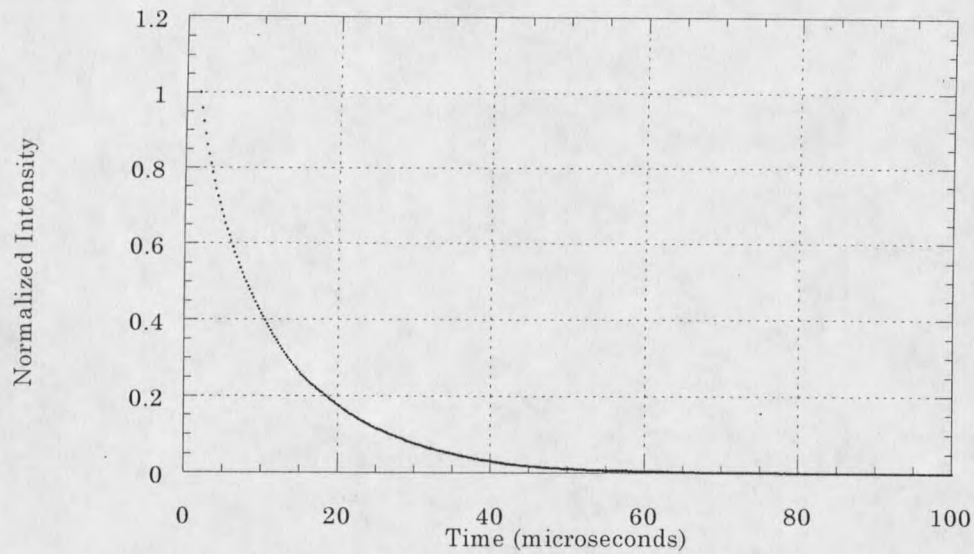


Figure 29. Decay (top) and Log of Intensity of Emission Transitions Originating from the $^4S_{3/2}$ Manifold in 4% Er:YAG.

transitions were observed in 0.5% Er:LuAG as in the other materials studied. Since the temporal behavior of the emission transitions in Er:LuAG was close to that in Er:YAG, the same experimental parameters were used in the Er:LuAG experiments as in the Er:YAG experiments. Details of the results for each of the emission transitions follow.

The integrated ${}^4I_{13/2} \rightarrow {}^4I_{15/2}$ transition shown in Figure 30 shows that this transition also occurs on the millisecond time scale. The signal was weaker for this material than in the other materials studied due to the lower (0.5%) erbium concentration, resulting in decreased signal-to-noise. This decay was also found to be exponential with a lifetime of 5.7 milliseconds.

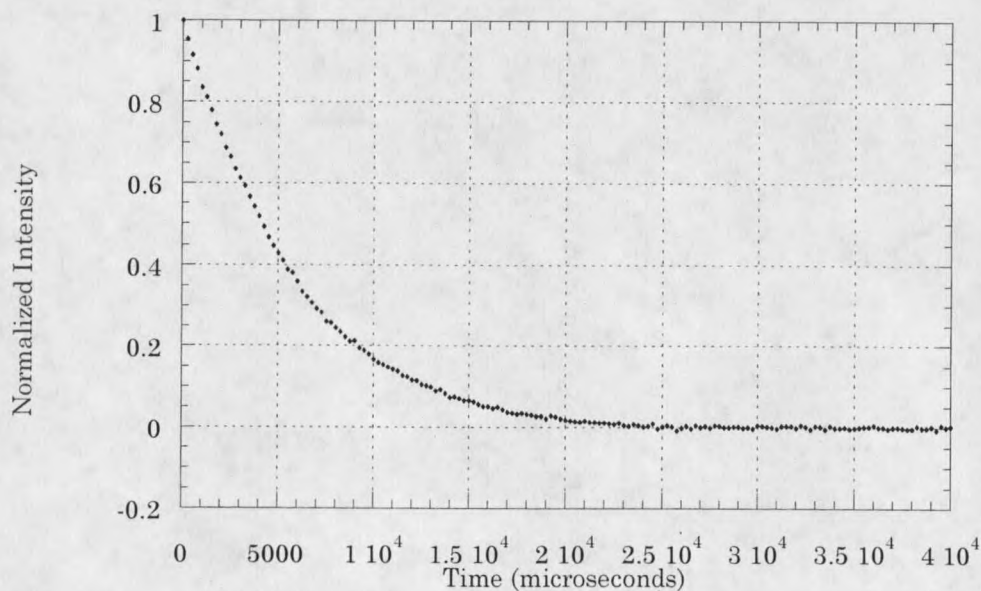


Figure 30. Decay of the ${}^4I_{13/2} \rightarrow {}^4I_{15/2}$ Transition for 0.5% Er:LuAG.

Figure 31 shows integrated decay and log plots for the ${}^4I_{11/2} \rightarrow {}^4I_{15/2}$ transition, following excitation to the ${}^4I_{11/2}$ manifold. The temporal behavior of the ${}^4I_{11/2} \rightarrow {}^4I_{13/2}$ transition is similar, but the signal-to-noise ratio is slightly lower due to the lower signal intensity of the transition. The experimental lifetime is 67.7 microseconds, and the log plot is, again indicative of exponential behavior.

The three infrared emission transitions initiated from the ${}^4S_{3/2}$ level were also observed in the Er:LuAG sample. The integrated trace of the transition terminating at the ${}^4I_{13/2}$ manifold is shown in Figure 32. This emission occurred after direct excitation to the ${}^4S_{3/2}$ manifold. The log plot showed the emission decay to be exponential, and the exponential fit on the decay data yielded a calculated lifetime of 12.3 microseconds. Attempts to obtain the visible emission spectrum after excitation to the ${}^4F_{7/2}$ manifold failed due to the relatively low signal strength of the low concentration sample and saturation of the silicon diode detector by the excitation pulse. However, this visible transition could be seen by the eye.

The rise time of the ${}^4I_{13/2} \rightarrow {}^4I_{15/2}$ transition has a exponential rise time similar to that of the ${}^4I_{11/2} \rightarrow {}^4I_{13/2}$ decay lifetime, indicating that the main channel of population of the ${}^4I_{13/2}$ level is through the ${}^4I_{11/2}$ level. The rise for all three materials studied is shown in Figure 33.

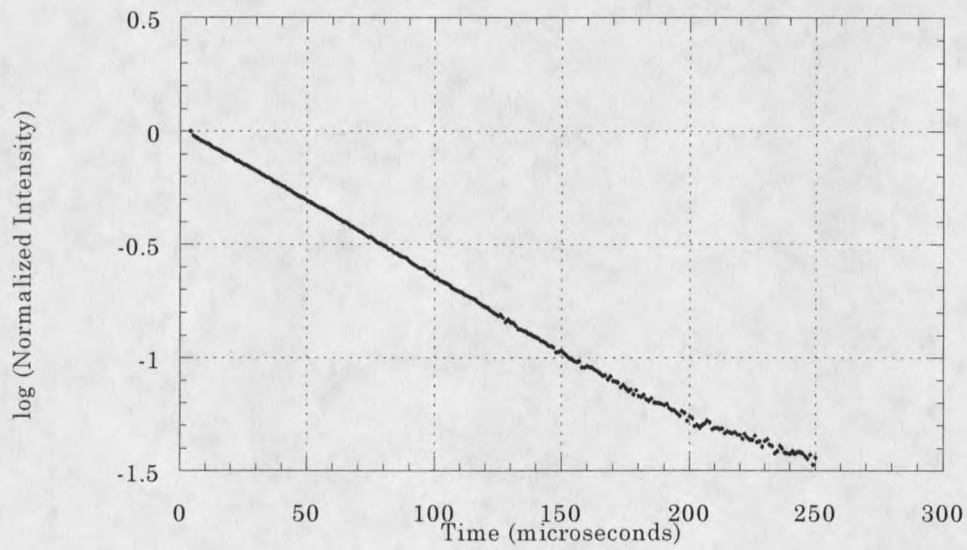
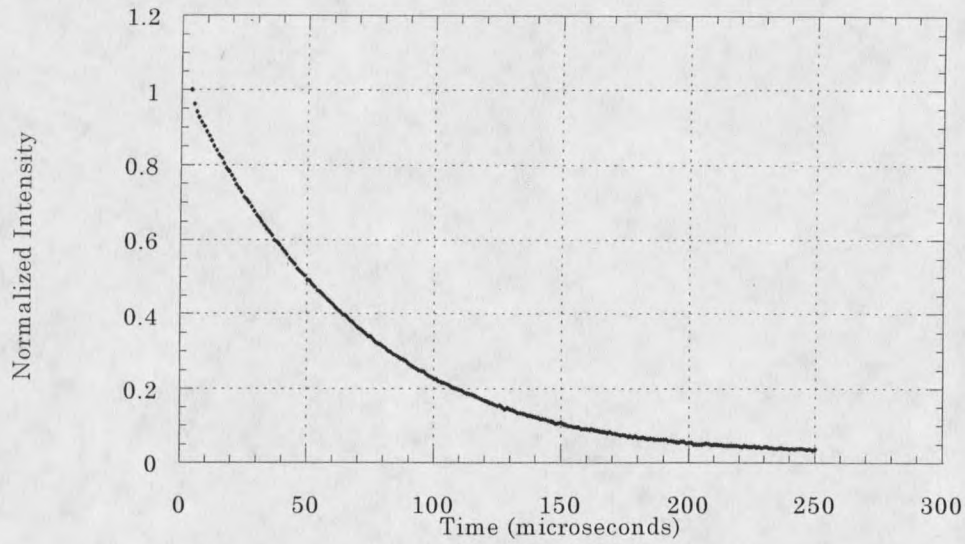


Figure 31. Decay (top) and Log of Intensity of the ${}^4I_{11/2} \rightarrow {}^4I_{15/2}$ Transition in 0.5% Er:LuAG.

